

# Geochemistry, Geophysics, Geosystems®



## RESEARCH ARTICLE

10.1029/2023GC011112

### Key Points:

- Basalt-hosted fault petrology records progressive stages of fluid-rock alteration followed by dissolution-precipitation cycles of cement
- The main mobile elements are Ca, Si, Al, and CO<sub>2</sub>, which are largely reprecipitated as Ca-zeolites and calcite within the fault zone
- Alternating calcite-zeolite mineralization highlights carbonate activity and metal cation availability feedback during fluid-rock reaction

### Supporting Information:

Supporting Information may be found in the online version of this article.

### Correspondence to:

B. Bamberg,  
bobbamberg@gmail.com

### Citation:

Bamberg, B., Reichow, M. K., Walker, R. J., & Ougier-Simonin, A. (2023). Petrological evolution and mass redistribution in basaltic fault zones: An example from the Faroe Islands, North Atlantic Igneous Province. *Geochemistry, Geophysics, Geosystems*, 24, e2023GC011112. <https://doi.org/10.1029/2023GC011112>

Received 10 JUL 2023  
Accepted 25 NOV 2023

### Author Contributions:

**Conceptualization:** Marc K. Reichow, Richard J. Walker, Audrey Ougier-Simonin  
**Data curation:** Bob Bamberg  
**Formal analysis:** Bob Bamberg  
**Funding acquisition:** Marc K. Reichow, Richard J. Walker, Audrey Ougier-Simonin

© 2023 The Authors. *Geochemistry, Geophysics, Geosystems* published by Wiley Periodicals LLC on behalf of American Geophysical Union. This is an open access article under the terms of the [Creative Commons Attribution-NonCommercial License](https://creativecommons.org/licenses/by-nc/4.0/), which permits use, distribution and reproduction in any medium, provided the original work is properly cited and is not used for commercial purposes.

## Petrological Evolution and Mass Redistribution in Basaltic Fault Zones: An Example From the Faroe Islands, North Atlantic Igneous Province

Bob Bamberg<sup>1</sup> , Marc K. Reichow<sup>1</sup>, Richard J. Walker<sup>2</sup>, and Audrey Ougier-Simonin<sup>3</sup> 

<sup>1</sup>School of Geography, Geology and the Environment, University of Leicester, Leicester, UK, <sup>2</sup>Department of Earth and Planetary Sciences, University of California, Davis, Davis, CA, USA, <sup>3</sup>Rock Mechanics and Physics Laboratory, British Geological Survey, Nottingham, UK

**Abstract** Fault rock petrology exerts an important influence on the permeability structure and mechanical properties of fault zones. Slip-related deformation on upper-crustal faults in basaltic rocks is closely associated with fluid-rock interaction, altering the distribution of physical properties within the fault. Here, we present quantitative descriptions of the geochemical and petrological evolution of basalt-derived fault rocks from three passively exhumed fault zones in the Faroe Islands. Fault-rock petrology is determined by optical petrography and automated phase identification based on micrometer-scale chemical maps from scanning electron microscope X-ray spectroscopy. Geochemical evolution is assessed from major and trace element composition measured by X-ray fluorescence. The fault rocks show intense fluid-mediated alteration from a tholeiitic basalt protolith in the damage zones, and mechanical mixing in the fault cores. Pervasive alteration occurs early during fault zone evolution, with incipient fault damage increasing permeability and allowing along-fault percolation of carbonated meteoric water, increasing fluid-rock ratios. Our results suggest that the only mobile species within the fault zones are Ca, Si, and Al, which are leached during the hydrolysis of volcanic glass and plagioclase, and CO<sub>2</sub>, which is added by percolating waters. These species are transported from the damage zones into the fault cores, where they precipitate as zeolite and calcite cement in veins and hydrothermal breccias. We propose that solutes are replenished by cement dissolution through pressure-solution during cataclastic creep, during repeated cycles of hydrofracture and cementation. The fault zones are natural reactors for fluid-mediated alteration by CO<sub>2</sub> and water, while other species are redistributed within the fault zones.

## 1. Introduction

Basalt is the most common volcanic rock type on Earth (Winter 2001) and holds great potential to reduce CO<sub>2</sub> concentration in our atmosphere. Basalts can act as a major carbon sink through metal carbonation (Lewis et al., 2021; Matter et al., 2016; Snæbjörnsdóttir et al., 2020) or through intercrystalline adsorption (Stillings et al., 2023). Additionally, the commonly elevated geothermal gradients in basalt formations can be tapped to provide sustainable geothermal energy (Marieni et al., 2018). Faults constitute an important heterogeneity in basaltic sequences, and their stability and permeability are strongly controlled by fault-internal petrological evolution (Frolova et al., 2014; Walker, Holdsworth, Imber, et al., 2013). Basalt alteration through reaction with residual fluids is thought to start immediately after emplacement during the cooling process (e.g., Mattioli et al., 2016). Alteration commonly takes the form of partial plagioclase replacement (Schenato et al., 2003) and dissolution of volcanic glass and primary minerals, especially olivine, and precipitation of various clay and zeolite minerals, and sometimes calcite, in vesicles (Kristmannsdóttir, 1979; Mattioli et al., 2016; Triana et al., 2012). Early alteration with residual fluids immediately after emplacement is followed by an alteration with hydrothermal fluids, and/or meteoric or sea water (Alt & Honnorez, 1984; Frolova et al., 2014; Mattioli et al., 2016; Schenato et al., 2003). Petrological characterizations of fault zones within basalt are scarce but indicate much a more extensive alteration than in the surrounding host basalt (Walker et al., 2012; Walker, Holdsworth, Armitage, & Faulkner, 2013; Walker, Holdsworth, Imber, et al., 2013). Such pervasive alteration can have profound implications for fault zone permeability and stability, where interconnected and permeable zeolite veins, and impermeable clay networks may result in a mixed barrier-conduit permeability structure (Walker, Holdsworth, Armitage, & Faulkner, 2013; Walker, Holdsworth, Imber, et al., 2013). In addition, the pervasive replacement of frictionally strong feldspar-dominated assemblages by weaker zeolites (Frolova et al., 2014; Yukselen-Aksoy, 2010) or clay minerals (Boulton et al., 2014; Carpenter et al., 2016; Haines et al., 2013; Shimamoto & Logan, 1981) can

**Investigation:** Bob Bamberg  
**Methodology:** Bob Bamberg, Marc K. Reichow  
**Project Administration:** Marc K. Reichow, Richard J. Walker  
**Supervision:** Marc K. Reichow, Richard J. Walker, Audrey Ougier-Simonin  
**Visualization:** Bob Bamberg, Richard J. Walker  
**Writing – original draft:** Bob Bamberg  
**Writing – review & editing:** Bob Bamberg, Marc K. Reichow, Richard J. Walker, Audrey Ougier-Simonin

promote mechanical weakening of the fault zone. The structure of the faults analyzed in this study also indicates that fault stability is strongly controlled by fluid pressure evolution and thus permeability structure of the fault (Bamberg et al., 2022).

In this study, we seek to characterize the petrological and geochemical evolution within basalt-hosted fault zones, and integrate these into a conceptual physicochemical model for fault evolution in shallow basalts (Bamberg et al., 2022). Chemical mobility and mass balance within the fault are calculated from X-ray fluorescence whole rock geochemistry. The petrological evolution of the fault zone is reconstructed through optical petrography and high-resolution, automated phase mapping based on X-ray spectrometry in a scanning-electron microscope (a full method is available in the supplement). The results represent a semi-quantitative and qualitative exploration of element mobility and petrological evolution in basalt-hosted faults, rather than quantitative characterization of chemical fluxes. We sampled three exceptionally well-exposed fault zones in the Faroe Islands Figure 1, that span a displacement range from 30 m to, potentially, kilometer-scale (Bamberg et al., 2022), and cover a full transect of fault rocks, including undeformed protolith, damage zone, fault core, and principal slip zone. Our results indicate that the initial pervasive alteration in the damage zone combined with comminution through cataclasis during strain accumulation appear to promote the compartmentalization of the fault core, limiting subsequent petrological evolution to zeolite and calcite precipitation and dissolution without communication to external fluid sources.

## 2. Geology of the Faroe Islands

The Faroe Islands (Figure 1a) are an archipelago located on the European continental shelf of the NE-Atlantic Ocean, between the Shetland Islands and Iceland. Lava forming the Faroe Islands were emplaced in the Paleogene, during the initial outburst of the Icelandic Plume before the onset of Atlantic rifting, as part of the North Atlantic Large Igneous Province (Ritchie & Hitchen, 1996). Faulting in the Faroe Islands developed during rifting and opening of the NE-Atlantic Ocean. Five overprinting stages of faults and dykes record progressive counter-clockwise rotation of the horizontal extension vector, indicating the growth of a continental relay zone between the Aegir and Reykjanes Ridges (Bubeck et al., 2017; Walker et al., 2011). Finally, faults were reactivated as a result of post-breakup passive margin uplift (Gaina et al., 2009; Gernigon et al., 2012; Walker et al., 2011).

The Faroese stratigraphy is dominated by tholeiitic basalts of the Faroe Islands Basalt Group, which are subdivided into seven formations (Passey & Bell, 2007; Passey & Jolley, 2008), with a maximum total stratigraphic thickness of ca. 6.6 km (Figure 1b) (Chalmers & Waagstein, 2006; Passey & Bell, 2007; Waagstein et al., 1984).  $^{40}\text{Ar}/^{39}\text{Ar}$  (Hansen et al., 2002; Storey et al., 2007) and K/Ar and  $^{40}\text{Ar}/^{39}\text{Ar}$  (Waagstein et al., 2002) suggest emplacement between 60 and 55 Ma. The Faroes stratigraphy is summarized in Figure 1b and described in detail by Rasmussen and Noe-Nygaard (1970), Waagstein et al. (1984), and Passey and Jolley (2008). The faults described in this study are hosted in the extensive sheet lobes of the 3.3 km thick Beinivørð Formation (Í Botni fault zone: Figures 1b and 1d), the compound lavas of the <1.4 km thick Malinstindur Formation (Gøtugjógv and Selatrað fault zone: Figures 1b and 1c), and the simple lavas of the 900 m thick Enni Formation (Selatrað fault zone: Figures 1b and 1c). The younger basalts of the Malinstindur and Enni Formations (Figure 1b) have been subdivided geochemically into two main groups: MORB-derived, low-Ti lavas ( $\text{TiO}_2 < 1.95 \text{ wt.}\%$ ) depleted of incompatible elements, and plume-derived, high-Ti lavas ( $\text{TiO}_2 > 1.95 \text{ wt.}\%$ ) with enriched incompatible element abundances (Gariépy et al., 1983; Hald & Waagstein, 1991; Holm et al., 2001; Søger & Holm, 2009). Both types are dominated by plagioclase-phyric basalts, but low-Ti basalts have on average 4% higher MgO and a small proportion are olivine-phyric basalts or picrites (Hald & Waagstein, 1991; Holm et al., 2001). A few less-common basalts have also been described, with either intermediate Ti concentration, high Ti and high Mg (>10%), or contaminated with lower crustal material (Holm et al., 2001). The Malinstindur Formation, hosting the Gøtugjógv fault zone and parts of the Selatrað fault zones, is dominantly composed of plagioclase-phyric high-Ti basalts (Holm et al., 2001; Søger & Holm, 2009). In the north of the archipelago, the Enni Formation, which is also cut by the Selatrað fault zone, is dominated by phyric and aphyric low-Ti basalts in the lower parts, and both aphyric high-Ti and low-Ti basalts in its upper part.

## 3. Structural Framework

The three fault zones analyzed in the Faroe Islands comprise up to decameter-wide damage zones, surrounding meter-wide fault cores that contain multiple cataclastic shear bands and lenticular breccia pods, organized around a central principal slip zone. Fault architecture is described in detail in Bamberg et al. (2022), including fault and fracture distribution, geometry, and deformation mechanisms. Hence, we summarize those aspects here before focusing

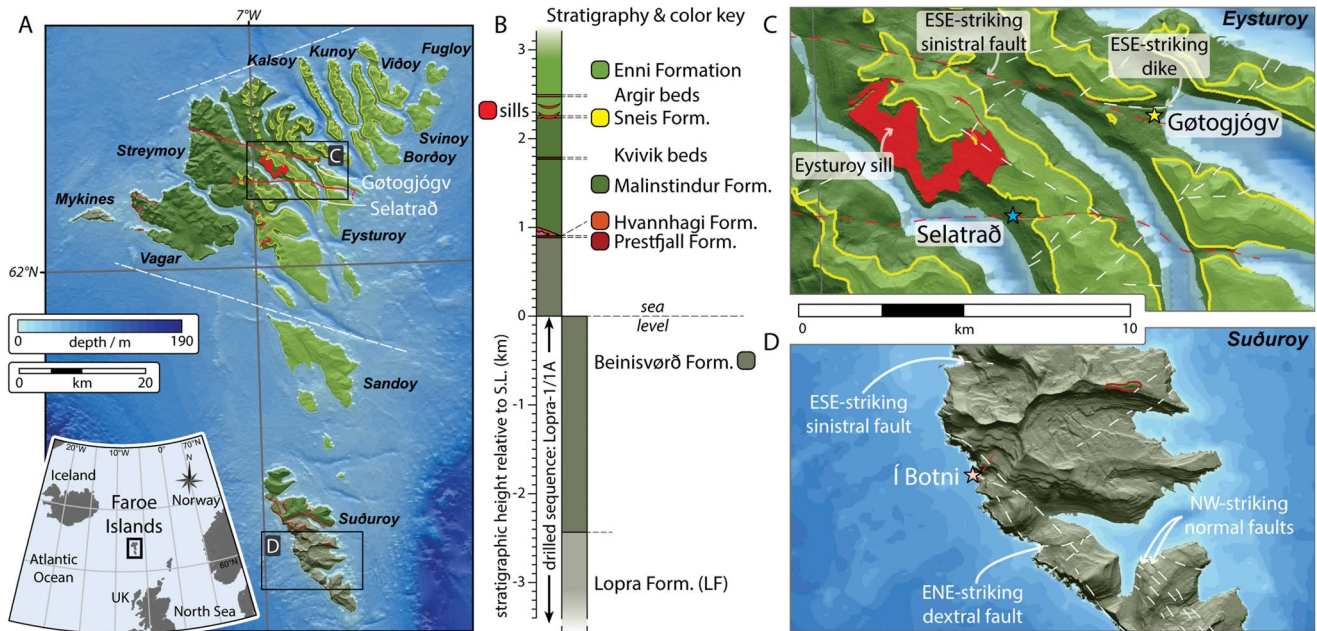


**Figure 1.** (a) Geological map of the Faroe Islands. White, dashed lines indicate the proposed locations of large displacement ENE-WSW (unnamed north coast fault; Walker et al., 2011), and ESE-WNW (Passey, 2009) faults that bound the Northern Islands. (b) Vertical stratigraphic section through the Faroe Island Basalt Group (from Passey and Bell (2007)). Close-up maps highlight the local topography and geology of the (c) Gøtugjógv, Selatrað, and (d) Í Botni fault zones. See key in (b) Studied fault zones are traced in red, other lineaments in white.

on the petrological evolution below. The damage zone of the small-displacement fault zone in Í Botni (IBO: location in Figure 1d, detail in Figure 2) consists of a range of variably altered cataclastic breccias (Figure 2b) in contact with the fault core, grading back to undeformed host rock through a zone of chaotic, mosaic, and crackle breccias (fault rock classification from Woodcock & Mort, 2008) (Figures 2b and 2c). In the large-displacement Gøtugjógv (GOT: location in Figure 1c, detail in Figure 3) and Selatrað (SEL: location in Figure 1c, detail in Figure 4) fault zones, the damage zone is characterized by high concentrations of meter- to decameter-scale fractures and secondary faults. Cataclastic shear bands in the fault core are roughly fault-parallel layers containing altered basalt, fault rock, and/or mineral cement fragments in a heavily comminuted matrix. The most prominent of these shear bands that does not show overprinting by younger structures were identified as the principal slip zone. Shear bands surround lenticular breccia pods of variable clast concentration that are mineralized with blocky calcite or idiomorphic zeolite (Figures 3b and 3c). Clasts can preserve the damage zone texture but show higher degrees of mineral alteration, or more frequently, are fragments of fault rocks and/or mineral cement. These breccia pods become more abundant and extensive with increasing distance from the principal slip zone. Shear bands further away from the principal slip zone tend to be brecciated and mineralized with zeolite and/or calcite (Figure 3e), representing an intermediary state between the active shear zone and the breccia pod. Moreover, fault cores are cut by fault-parallel tabular veins of up to decameter apertures and mineralized with the same blocky calcite or idiomorphic zeolite found in breccias.

Bamberg et al. (2022) interpreted these structures as evidence for repeated principal slip zone migration and fault core reorganization with intermittent hydrofracture events, where: (a) Permeability reduction in a cataclastic shear band leads to fluid pressurization, triggering hydrofracture and widespread mineralization of the fault core with mechanically strong calcite and zeolite cement; (b) Strengthening forces strain localization into weaker structures of the core, establishing a new principal slip zone; and (c) continued slip leads to older, abandoned structures becoming reworked into the new slip zone.

## 4. Results

### 4.1. Fault Zone Meso- and Microtexture

The unmodified host rock in all localities is tholeiitic basalt dominated by plagioclase-pyroxene assemblage including abundant ilmenite and magnetite (Figures 5a, 6a, and 6b). The compound lava hosting the Gøtugjógv

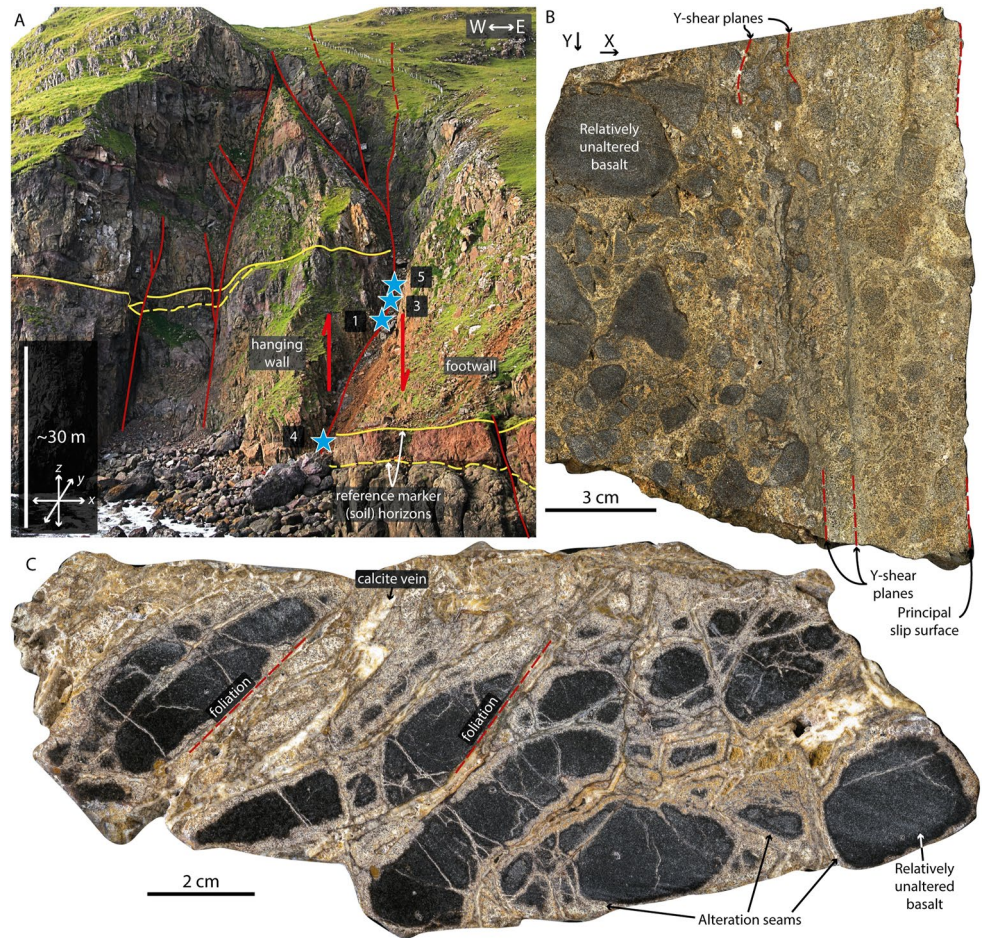


**Figure 2.** (a) The I Botni fault zone on Suðuroy is a 50 m wide normal fault with 30 m displacement concentrated on the easternmost strand, as indicated by the marker horizon (yellow). Sample locations are indicated by blue stars. (b) IBO1-3) The fault core (footwall portion preserved on the righthand side of the sample) is bounded by slip surfaces and cataclastic, chaotic breccias coarsening away from the core. (c) IBO1-4) Alteration is limited to the immediate wall rock of fractures and cracks, and rare calcite cements. Localized, black foliation might indicate pressure-solution.

and Selatrað faults can contain <1 cm sized plagioclase phenocrysts, which are absent from the simple lava in Í Botni. The fine-grained groundmass is composed of opaques (identified as ilmenite and magnetite by SEM-EDS; Figures 6a and 6b), 50–100  $\mu\text{m}$  glomerates of anhedral pyroxenes, 100–500  $\mu\text{m}$  long euhedral plagioclase crystals, as well as 50–100  $\mu\text{m}$  sized subhedral olivine crystals. The latter have been almost fully replaced by brown, amorphous to fibrous iddingsite  $\pm$  chlorite (Figures 5a and 5b). Abundant pockets of brown volcanic glass form an intersertal texture with the plagioclase crystals. The volcanic glass is partially devitrified, often showing radially fibrous rims of a light brown color, enclosing a green-brown interior with dark-green interference colors (likely representing palagonite), and sometimes a core of zeolite (Figures 5a and 5c). Vesicles, most abundant in the porous lava tops, tend to be lined with <50  $\mu\text{m}$  of celadonite  $\pm$  clay minerals and are filled with coarse zeolite ( $\leq 500 \mu\text{m}$ ; Figures 5g and 6c). Optically estimated mineral abundances are 30% plagioclase, 35% pyroxene, 5% opaques, 10% olivine and alteration products, and 20% (devitrified) volcanic glass.

Within the fault damage zones, plagioclase crystals show an increasing concentration of intracrystalline fractures toward the fault core, which are zeolitized as deep as a few micrometers (Figure 5d). In the vicinity of veins and large-scale fractures, plagioclase breakdown becomes more extensive, with complete replacement in some cases (Figures 5f and 5g). In early stages of faulting, as shown in Í Botni, the damage zone is brecciated approaching the principal slip zone, grading from mosaic to chaotic breccia at the slip zone contact, with centimeter-scale clasts in a comminuted matrix, and in some places, calcite cement (Figures 2b and 2c). The  $\leq 50$  cm wide slip zone itself is bounded by striated and polished slip surfaces. It is dominated by gouge and cataclasite, with

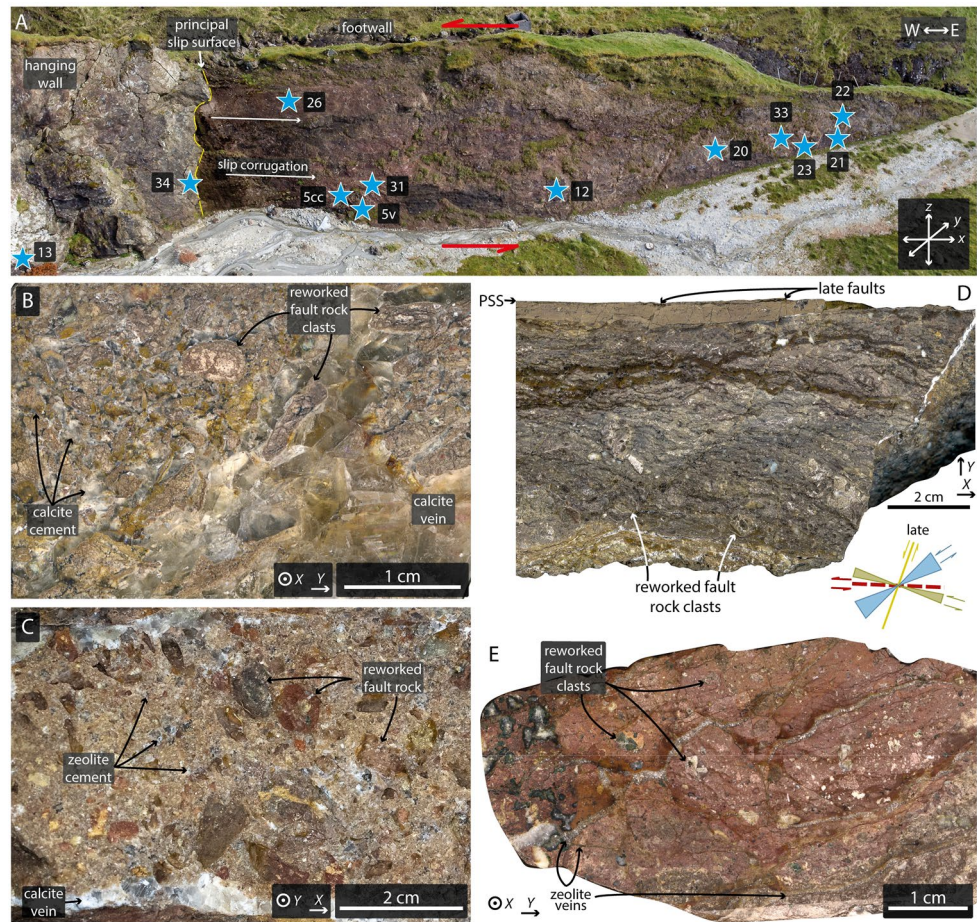


**Figure 3.** (a) A 50-m-long and 10-m-high diagonal section through the fault core of a sinistral strike-slip fault zone is exposed near Gotugjogv. The corrugated principal slip surface (corrugation plunge shown by arrows) encloses a slip zone of lenticular bodies containing fault rock and bounded by cataclasites. Sample locations are indicated by blue stars. Samples from the fault core also host extensive (b: GOT12) calcite- and (c: GOT5v) zeolite-cemented fault veins that run parallel to the slip surface with angular fault rock fragments. Panel (d: hanging wall slip surface, not analyzed) Cataclasites of the slip surface in some cases are strongly foliated, and show late-stage faults cutting the main foliation. Panel (e: GOT5cc) Cataclastic bands away from the principal slip surface show signs of reworking, such as brecciation by zeolite veins. Clasts of reworked fault rock are common throughout the fault core.

weakly altered host rock clasts (Figures 2b and 2c), commonly up to a 5 mm in diameter but sometimes as large as 1–2 cm, in a fine-grained matrix (<25  $\mu\text{m}$ ). Clast composition and microtexture are similar to the damage zone rocks described above, with preserved basaltic texture, including fractured and partially zeolitized plagioclase. The matrix is composed of altered host rock that is comminuted to the micrometer scale. Optical discrimination between plagioclase and zeolite in the fine-grained matrix is only possible where plagioclase feldspars display distinctive polysynthetic twinning inhibiting an accurate estimation of the degree of zeolitization. However, albite twins can be observed in some matrix grains, indicating that plagioclase zeolitization is not complete. Further, a brown microcrystalline-amorphous or fibrous phase is common along fractures, resembling iddingsite replacing olivine. The degree of plagioclase zeolitization can be quantified using SEM-EDS and is described in the next section.

In larger displacement faults (the Götugjógv and Selatrað fault zones), small-scale brecciation, as seen in Í Botni, is rare within the damage zone. Instead, the altered host rock described previously is fractured by meter- to decameter-scale secondary faults and smaller fractures, some of which are mineralized with calcite and/or zeolite closer to the fault zone. The fault cores are composed of fault rock lenses bounded by cataclastic shear bands organized around a prominent slip surface (Figures 3a and 4a). These lenses usually contain cataclasites proximal to the slip surface (Figure 3e), and mineralized breccias closer to the damage zone (Figures 3b and 3c). The shear bands

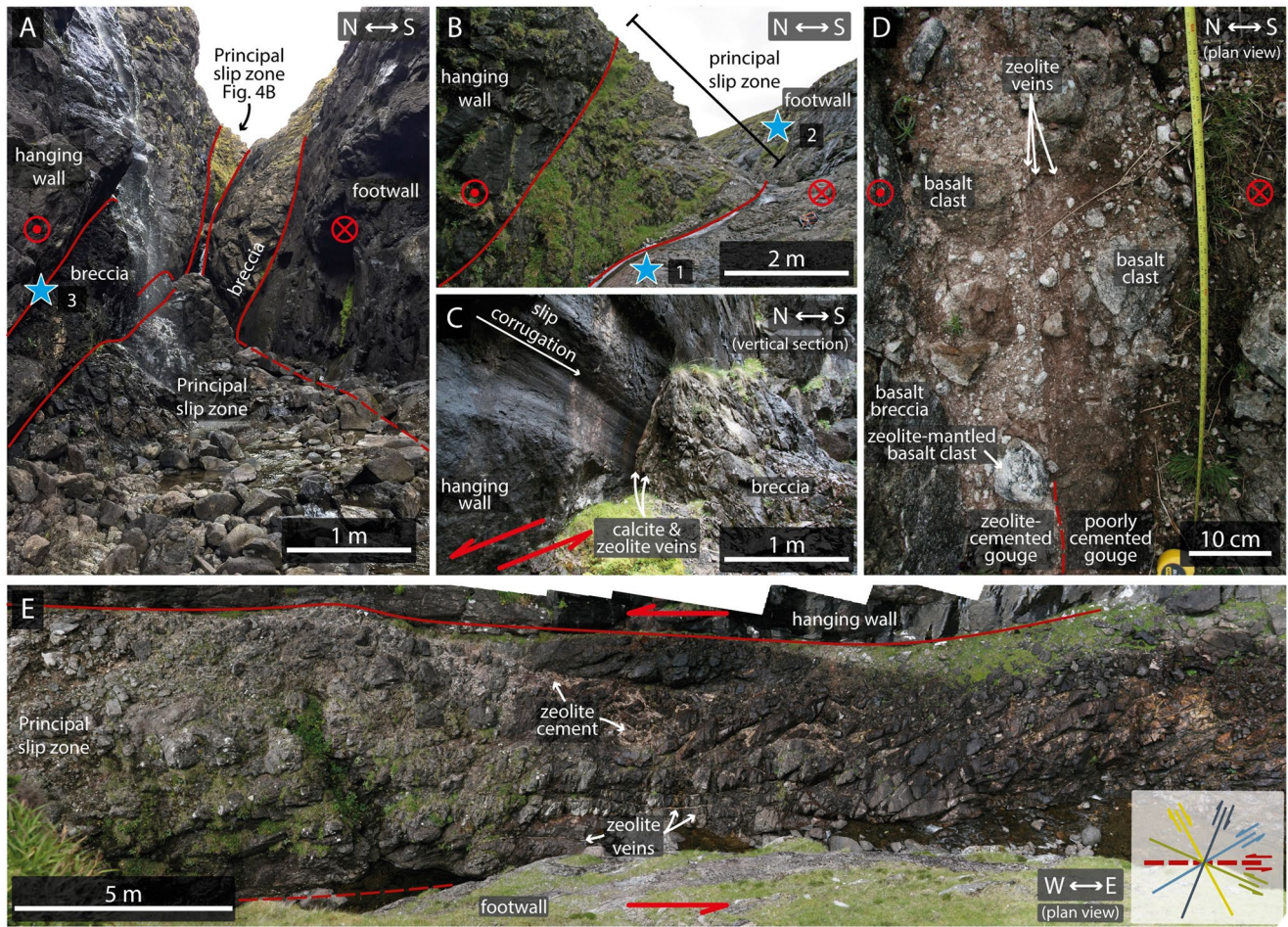


**Figure 4.** (a) The sinistral strike-slip fault zone at Selatrad is exposed in a deep and long canyon, where a stream has eroded the fault core. Several (a) and (b) fault rock lenses and (c) polished and striated slip surfaces can be identified. (d) and (e) The canyon floor shows the fault core with a decameter-thick principal slip surface composed of partially cemented gouge in the north, next to a (e) highly fractured (following Riedel orientations) meter-thick layer in the south.

are composed of ultracataclasite (or gouge) as is a <10 cm thick zone around the slip surface (Figures 3d, 4d, 5i, and 5j). Clasts within the breccia tend to preserve primary basaltic textures, with pyroxene glomerates that show little evidence of alteration despite intense fracturing, and glass in the interstitial space is replaced by opaques, zeolites, and diffuse patches of dark red-brown staining over microcrystalline grains and spherulitic–dendritic opaques (identified as ilmenite by SEM-EDS) (similar to the proximal damage zone; Figures 5c and 5h). Some clasts are composed of other fault rocks—breccias or cataclasites—and in some cases contain multiple types of fault rock separated by a sharp contact, such as clast-within-clast textures or fragments of wall-rock–vein contacts (Figures 5n–5p). These clasts are mostly hosted in well crystallized, millimeter-long bladed zeolite (Figure 5n) and/or <0.5 mm blocky calcite cement (Figures 5o and 5p). The pore space within the zeolite cement is filled with a single crystal ( $\leq 1$  cm) calcite (Figure 5n). In calcite-cemented breccias, clasts are commonly overgrown with a thin zeolite coating of irregular thickness (<1 mm) (Figure 5o), and the cement also contains pockets of zeolite with the contact either following an idiomorphic calcite grain boundary, or showing calcite growth around the zeolite crystals; sometimes both styles are developed in the same pocket (Figure 5p).

Many cataclasites in Götugjógv and Selatrad are foliated on hand-specimen scale, featuring millimeter-wide dark red-brown bands parallel to Riedel shear orientations (Figure 3d), and manifesting through a diffuse staining of the matrix on the microscale (Figure 5l). Additionally, some cataclasites show microscopic foliation of aligned, light brown-yellow clay bands separating other grains (Figure 5k). Breccias from Í Botni can contain very narrow black foliae between clasts that resemble pressure-solution seams (Figures 2c and 5e). The cataclasite matrix is commonly stained to a dark red-brown color, and dominated by zeolite and clay minerals, mixed

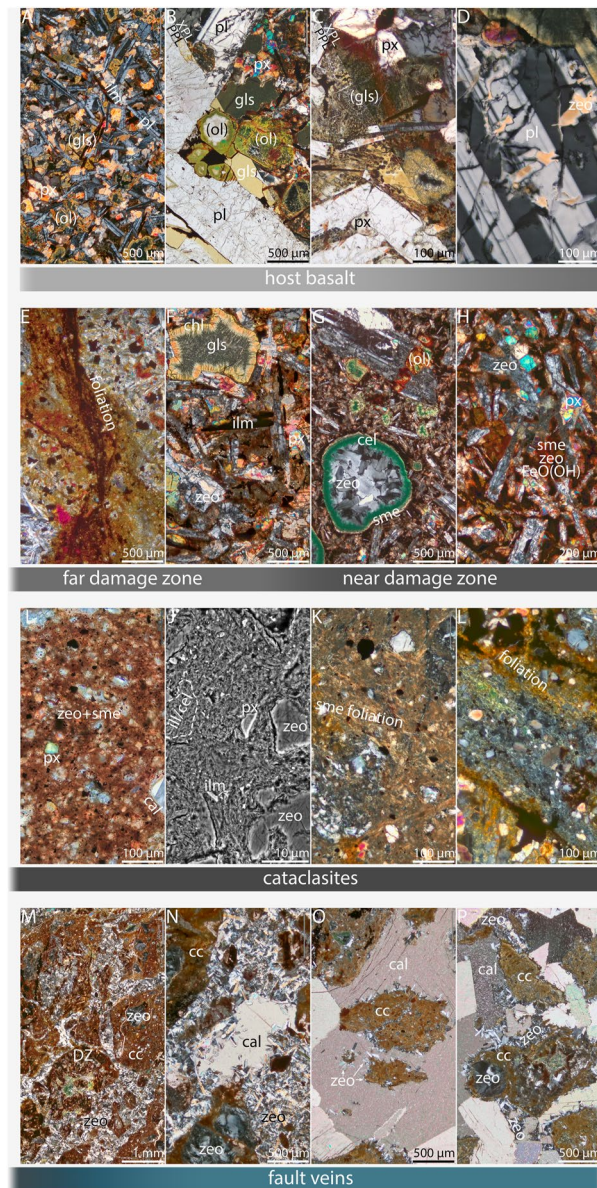


**Figure 5.** Petrography of basalt-derived fault rocks. (a: GOT13) Tholeiitic host basalt; (b: GOT13) close-up of plagioclase phenocryst with altered volcanic glass and pyroxene in interstitial space (XPL top, PPL bottom); (c: GOT13) secondary minerals derived from volcanic glass breakdown (XPL top, PPL bottom); (d: SEL2) zeolitization (brown) along intracrystalline cracks in plagioclase; (e: IBO1-4) localized dark foliation in Botni damage zone breccia; (f: SEL2) altered basalt in damage zone with prominent, devitrified glass (top right corner); (g: GOT21) celadonite- and heulandite-filled vesicles as well as altered olivine in plagioclase phenocryst; (h: GOT34) close-up of altered basalt with prominent zeolitized plagioclase laths and red stained interstitial space; (i: SEL1) highly comminuted and stained ultracataclastic matrix in slip zone; (j: GOT5cc) SEM-BSE micrograph of cataclastic matrix; (k: GOT26) pervasive, clayey foliation in cataclasite; (l: IBO1-3) some cataclasites show additional, wide foliation defined by diffuse Fe-staining; (m: GOT5cc) brecciated cataclasite with zeolite cement; (n: GOT5v) calcite filling pore in zeolite-cemented fault vein; (o: GOT12) zeolite overgrowth around clast preceding coarse calcite cementation; (p: GOT12) complex intergrowth of zeolite and calcite cements in fault vein. Cal, calcite; cc, cataclasite; cel, celadonite; chl, chlorite; DZ, damage zone; gls, volcanic glass [(gls): altered]; ilm, ilmenite; ol, olivine [(ol): altered]; pl, plagioclase; px, pyroxene; sme, smectite; zeo, zeolite.

with comminuted pyroxene (<25 μm) and opaques (<10 μm) (Figure 5i). High-magnification SEM-BSE micrographs of the cataclasite matrix show a mixture of angular fragments of zeolite and pyroxene, generally 1–5 μm in size, and a micrometer- to sub-micrometer-scale, very bright fragments of Fe- and/or Ti-oxides, suspended in a matrix with a platy and/or spongy texture and a grain size ≤2 μm, possibly representing clay minerals (Figure 5j).

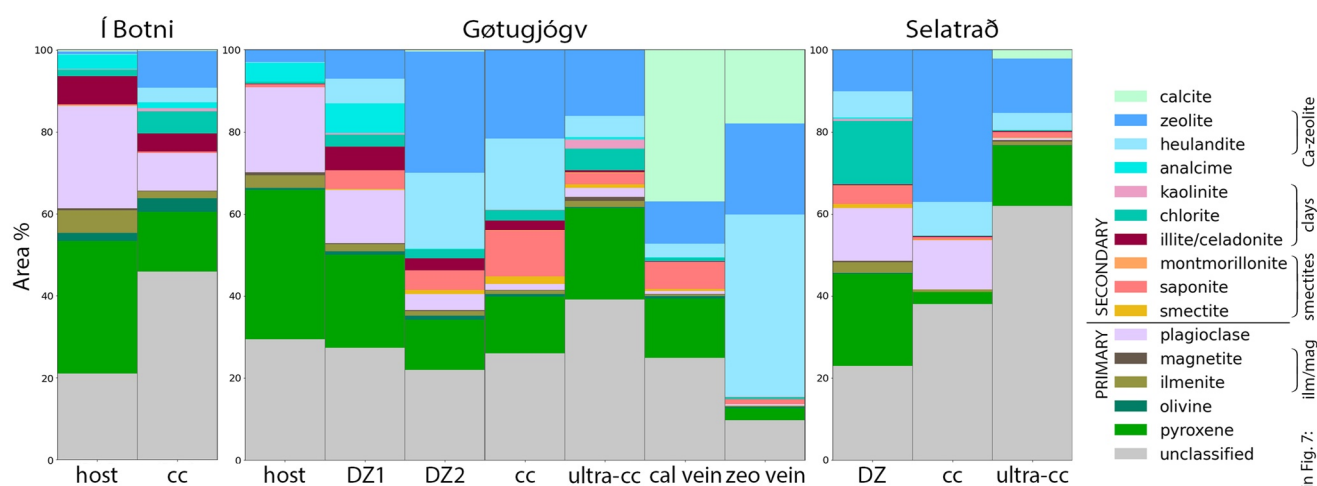


**Figure 6.** (a) SEM-EDS mineralogy. Cc, cataclasite; DZ, damage zone; vein, fault vein; zeo, zeolite. IBO host: IBOofwhost, cc: IBO1-3; GOT host: GOT13, DZ1: GOT34, DZ2: GOT21, cc: GOT5cc, ultra-cc: GOT 26, cal vein: GOT12, zeo vein: GOT5v; SEL DZ: SEL3, cc: SEL2, ultra-cc: SEL1.

Many clasts are made up of reworked mineral cement from veins and breccias, sometimes including the contact with the wall rock, but also other cataclasites, or even heavily altered host rock remnants with preserved basaltic texture and amygdalae (Figures 5m–5p). Ultracataclasites lining prominent slip surfaces are much more homogeneous and have smaller clasts than all other sampled (ultra-) cataclasites (Figures 5i and 5j). Some cataclasites further away from this slip surface are extensively fractured and brecciated by a network of non-tabular, well-mineralized zeolite ± calcite veins (Figure 5m).

#### 4.2. SEM-EDS Based Mineralogy

Mineral maps generated from automated phase identification, which were based on element concentrations mapped using EDS, reveal a strong spatial association between plagioclase and zeolite in host and damage zone rocks (Figure 6). Plagioclase grains appear variegated with a network of zeolites and an unclassified mineral phase (Figures 6b and 6c). Identified zeolites include analcime, most commonly in Gøtugjógv host rock and damage zone, heulandite (more common in the fault core, but also in the Selatrað damage zone sample), or an unspecified zeolite phase which occurs in all samples. Most of this unspecified zeolite phase matches the heulandite classification but with slightly elevated Na and/or reduced Si concentrations. Patches of unclassified material contain individual pixels identified as zeolite, which could indicate that these patches are a zeolitic phase that does not fit into the chemical bounds defined in our recipe (Table S1 in Supporting Information S1). In Í Botni, plagioclase is preserved even in very mature cataclasite next to the slip surface. However, both in Gøtugjógv and Selatrað plagioclase is virtually absent from the fault core ( $\leq 4\%$ ), while the zeolite concentration is markedly increased compared to the damage zone (Figure 6a).

Pyroxene concentration remains largely consistent after decreasing by about 10%–20% from host rock to damage zone (Figure 6a). This becomes particularly evident when corrections for varying abundances of vein and amygdale cements are taken into account (i.e., normalized to the area excluding heulandite, zeolite, and calcite, but including analcime from in situ plagioclase replacement). A notable outlier is the cataclasite sample from Selatrað, which has a large area of zeolite-cemented plagioclase fragments and reduced pyroxene concentration. Pyroxenes are disseminated throughout the fault rocks, and decrease in size in more mature rocks while maintaining a high angularity (Figures 5 and 6).

SEM-EDS identified most clay minerals in the samples as smectites (i.e., saponite, montmorillonite, or unspecified), illite/celadonite, chlorite, and rare kaolinite (Figure 6). Due to their identical chemical composition, SEM-EDS is unable to distinguish between celadonite and illite, which commonly incorporates Fe and Mg (Deer et al., 2013; Zviagina et al., 2020); hence, they are grouped together here. Illite/celadonite is mostly found in the rims of zeolite-filled amygdalae in the host rock and damage zone, but also disseminated through fault rocks, though at a very low abundance (Figures 6c and 6d). The bright green color visible in these zones under an

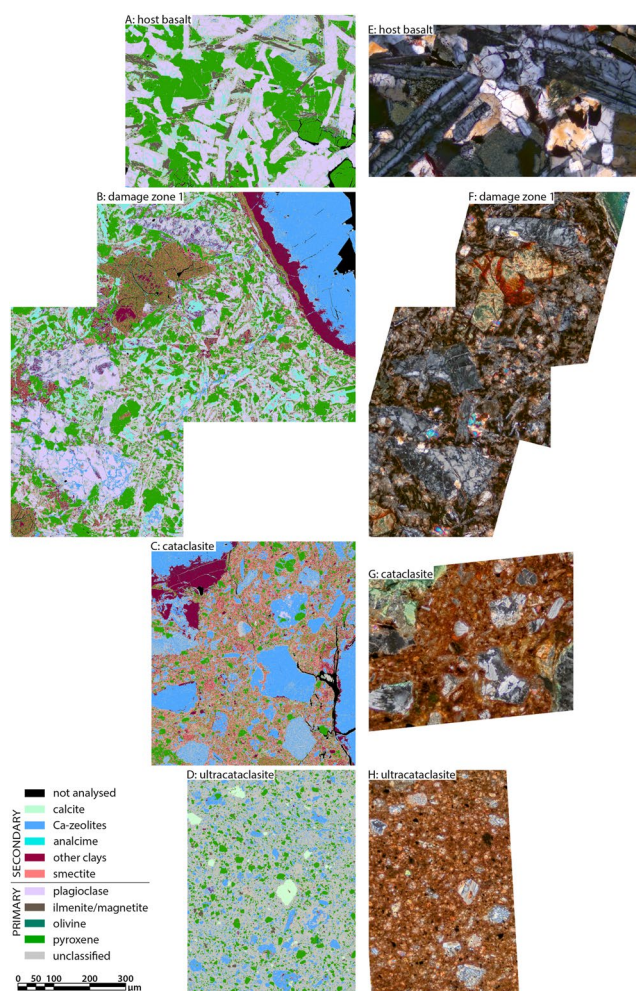


**Figure 7.** (a–d) SEM-EDS phase maps and (e–h) corresponding photomicrographs showing the evolution from host basalt to ultracataclasite in Gøtugjógv. Panel (e) is not the exact area mapped in (a) but shows similar texture and mineralogy from the same area of the thin section. (a and e: GOT13) Replacement of plagioclase with analcime in assimilated host rock, (b and f: GOT21) followed by analcime replacement with calcic heulandite, then (c and g: GOT5cc) textural breakdown in cataclasite and complete zeolitization and argillization of the cataclastic matrix, and finally (d and h: GOT26) intense comminution in ultracataclasite. The fine grain size of the latter inhibits reliable phase identification. All images share the same scale. Mineral phases have been grouped as indicated in Figure 6. An unsimplified version can be found in the Digital Supplement.

optical microscope indicates that the identified mineral is celadonite rather than illite (Figure 5g). Chlorite concentration is more stable throughout the fault, and it occurs either as an in situ alteration product of olivine or glass or disseminated in the rocks. Glass alteration is most notable in the Selatrað damage zone sample, which contains large (>50 μm) grain-shaped clusters of chlorite, while the most prominent example of olivine can be found in the Gøtugjógv damage zone sample (top left in Figure 6c). This altered olivine grain is composed of a fine-grained mixture of chlorite, illite, and saponite and displays the characteristic intracrystalline cracking of olivine. Measured concentrations of smectites were relatively low in all samples (Figure 6a). Mineral mapping only reveals significant concentrations of saponite in one sample, but as mentioned above, the texture in high magnification BSE micrographs shows the typical platy and/or spongy texture of clay minerals with grain sizes ≤2 μm (Figure 5j). We discuss the quality of SEM-based mineral mapping in the digital supplement.

### 4.3. Fault Rock Geochemistry

#### 4.3.1. Whole Rock Major and Trace Element Composition (XRF)

The plagioclase-pyroxene to zeolite-smectite-pyroxene mineralogy of the samples is reflected in their major elemental whole rock composition, dominated by SiO<sub>2</sub>, Al<sub>2</sub>O<sub>3</sub>, CaO, Fe<sub>2</sub>O<sub>3</sub>, and MgO, and minor amounts of Na<sub>2</sub>O, K<sub>2</sub>O, and TiO<sub>2</sub> (Table 1 and Figure 8). All figures plot anhydrous composition, that is, re-normalizing major elements to 100 wt.%.

Whole rock chemical composition of our samples falls on a trend from high-Ti basalt composition toward an ideal clinoptilolite-Ca endmember (Figure 8). The protolith and damage zone samples that were the furthest removed from the fault zone, as well as some cataclasite samples coincide with the composition reported for high-Ti basalts in the Faroe Islands (e.g., Holm et al., 2001; Søger & Holm, 2011), while (fault) veins are close to the clinoptilolite-Ca endmember, with compositions of breccias ranging in between. The spread in data observed in our samples is distinct from element distributions observed in Faroe Island basalts and evolutionary trends related to the process of fractional crystallization (e.g., high Al<sub>2</sub>O<sub>3</sub> and CaO contents), as illustrated in Figure 8. The chemical composition remains largely unchanged throughout the fault zone (Figure 9), the only major excursions being samples with abundant calcite (IBO1-1 and GOT12) or zeolite cement (GOT23 and GOT5v). Due to the small number of samples from Í Botni and Selatrað, the following description will focus mainly on samples from Gøtugjógv. The patterns described there are reflected in the data from the other two fault zones.

The protolith samples selected as a reference for further analysis are the most pristine rocks that were accessible close to the fault outcrops, and fall within the typical basalt composition reported for the Faroe Islands (Figure 10).

They are averaged Í Botni hanging wall and footwall host rock (samples IBOhwhost and IBOfwhost), Gøtugjógv hanging wall host rock (GOT13, Figures 5a and 5c), and the relatively unaltered wall rock from a distal damage zone fracture in Selatrað (SEL2, Figures 5b and 5d). Petrographic analysis and SEM-EDS mineralogy (Figure 6) of the Í Botni host rock samples show fully preserved basaltic assemblage with unaltered calcic plagioclase, pyroxene, glass, and opaques, but olivine has been replaced with iddingsite. The Gøtugjógv and Selatrað samples show minor plagioclase alteration along intracrystalline fractures as well as partial glass breakdown (Figures 5a–5d).

We assess element mobility in the faults by comparing the fault rock composition to the local protolith using isocon diagrams (Figure 11) (Ague, 1991; Grant, 1986; Hippert, 1998). Figure 7 reveals that Zr, and to a lesser extent TiO<sub>2</sub>, MgO, Cu, and Zn remain immobile during fault rock deformation. We therefore used Zr in the

**Table 1**  
*Bulk Rock Composition (Major Elements) of Selected Fault Rock Samples in Weight Percentage Recalculated to 100% (Incl. LOI)*

Sample	Rock type	SiO <sub>2</sub>	TiO <sub>2</sub>	Al <sub>2</sub> O <sub>3</sub>	Fe <sub>2</sub> O <sub>3</sub>	MnO	MgO	CaO	Na <sub>2</sub> O	K <sub>2</sub> O	P <sub>2</sub> O <sub>5</sub>	SO <sub>3</sub>	LOI
GOT13	Host	47.60	2.68	13.54	13.21	0.17	6.52	10.61	2.28	0.22	0.22	0.10	2.85
GOT34	HW DZ	46.06	2.92	11.21	14.19	0.17	6.92	8.97	2.15	0.35	0.24	0.10	6.71
GOT21	FW DZ	49.68	2.12	14.43	11.79	0.11	4.71	7.46	2.77	1.11	0.20	0.10	5.52
GOT22	Breccia	49.04	2.32	12.05	11.03	0.20	5.04	8.66	1.06	0.41	0.20	0.10	9.90
GOT31	Proto-cc	55.27	1.65	14.85	9.73	0.15	2.92	12.15	0.75	0.22	0.17	0.10	2.03
GOT33	cc	47.11	1.66	15.53	8.73	0.11	4.24	11.57	1.45	0.47	0.16	0.10	8.87
GOT20	cc	53.06	1.37	13.84	7.48	0.07	3.01	7.23	0.84	0.25	0.12	0.10	12.62
GOT5cc	Ultra-cc	48.91	1.98	13.47	10.08	0.16	4.38	9.05	0.93	0.29	0.17	0.10	10.49
GOT26	Ultra-cc	46.69	2.31	13.64	11.88	0.20	5.39	9.79	1.46	0.32	0.20	0.10	8.03
GOT23	Zeo vein	57.82	0.24	17.06	1.28	0.02	0.36	8.17	1.38	0.05	0.02	0.10	13.50
GOT5v	Zeo vein	48.98	0.45	12.89	2.27	0.04	0.59	14.86	0.56	0.06	0.06	0.10	19.14
GOT12	Cal vein	11.29	0.36	2.67	2.31	0.09	0.57	45.94	0.12	0.05	0.05	0.10	36.44
IBOHwhost	HW host	47.00	3.76	12.78	16.92	0.24	5.36	9.51	2.72	0.35	0.38	0.10	0.88
IBOFwhost	FW host	47.09	3.28	13.59	15.94	0.21	5.18	9.49	3.24	0.75	0.33	0.10	0.79
IBO1-4	Breccia	39.97	2.64	9.98	14.72	0.16	5.16	12.32	1.82	0.58	0.26	0.10	12.28
IBO1-3	Proto-cc	47.03	3.35	13.11	15.98	0.20	4.87	9.93	2.95	0.70	0.33	0.10	1.45
IBO1-1	cc	28.03	1.15	7.92	6.89	0.13	1.39	25.27	1.28	1.36	0.08	0.02	26.47
IBO1-5	Gouge	46.86	3.33	13.14	16.16	0.20	4.96	9.91	2.95	0.68	0.33	0.10	1.39
SEL2	Host	47.59	2.90	14.78	12.15	0.24	5.47	8.88	1.76	0.35	0.24	0.10	5.54
SEL3	DZ cc	44.74	2.38	16.91	9.68	0.11	3.48	9.42	1.92	0.23	0.22	0.10	10.80
SEL1	Ultra-cc	44.61	1.87	14.44	10.43	0.16	5.48	10.97	1.76	0.30	0.17	0.01	9.80
LLD		0.40	0.01	0.28	0.02	0.01	0.13	0.05	0.17	0.01	0.02	0.08	
RSD/%		0.6	0.4	1.5	0.3	49.4	0.3	0.3	3.2	1.5	2.0	48.3	

*Note.* Raw data in data repository (Bamberg, 2023). Cc, cataclasite; cal, calcite; DZ, damage zone; FW, foot wall; HW, hanging wall; LLD, lower limit of detection; RSD, relative standard deviation; vein, fault vein; zeo, zeolite.

following as a reference element to calculate global mass change (i.e., how much mass a unit of protolith lost or gained during chemical alteration: Figure 12) and element mobility (Figures 13 and 14). Global mass change (mass of the altered sample  $M^A$  vs. mass of protolith  $M^0$ ) can be calculated via the concentration of the immobile element in the altered sample  $C_i^A$  compared to the concentration of the immobile element in the protolith  $C_i^0$  using (Ague, 1991; Grant, 1986):

$$\frac{C_i^0}{C_i^A} = \frac{M^A}{M^0} \quad (1)$$

In Götugjógv, the relative mass change compared to host rock records a mass loss (−7%) in the damage zone, 0.5 m away from the fault core (GOT34) compared to protolith, and mass gains (ca. 23%) in the damage zone directly in contact with the core (GOT21), increasing to up to 105% in cemented breccias (GOT20), and returning to 23% in the ultracataclasite sample (GOT26). For the fault veins, total mass gain ranges between 490% (GOT5v) and 1,000% (GOT23). Selatrað shows a similar pattern with mass gain of 53% in the ultracataclasite (SEL1), while Í Botni shows a relative mass change within ~20%, where cement is absent, and up to 200%, where cemented with calcite (IBO1-1) (Figure 12).

Diagrams of element concentration plotted against immobile Zr for all samples show the mobility of individual oxides/elements undistorted by the effect of global mass change (Figures 13 and 14). Immobile elements plot on the isocon connecting the origin to the protolith. Samples that plot above the isocon have gained the relevant oxide (i.e., they are enriched), whereas samples that plot below the isocon are depleted relative to the host rock. The plots reveal

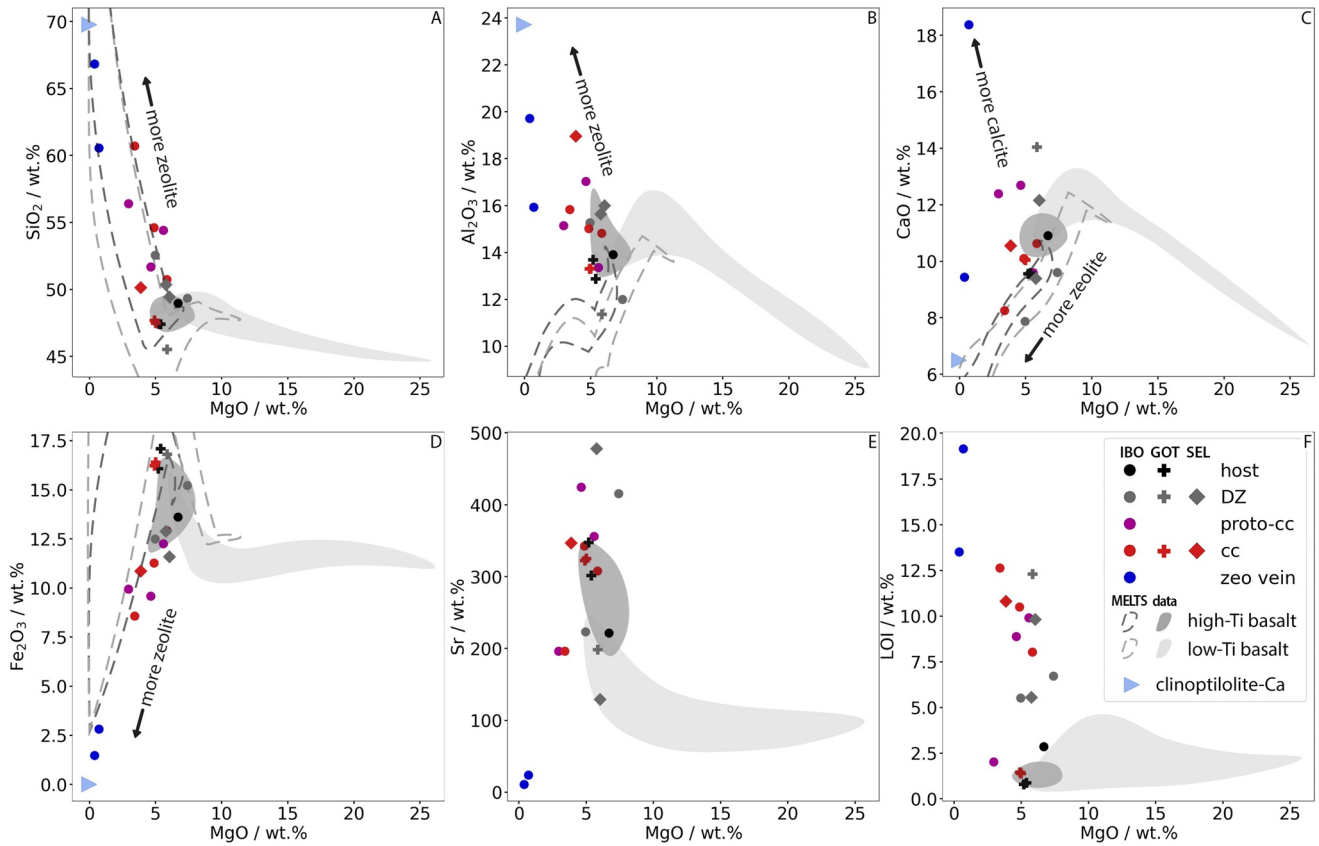


**Figure 8.** Harker plots showing basalt host and fault rock major and trace element composition. Note the general trend from undeformed high-Ti tholeiitic basalt toward clinoptilolite-Ca composition (blue triangle) in fault veins. The thermodynamic modeling program MELTS (Ghiorso & Sack, 1995; Gualda & Ghiorso, 2015; Gualda et al., 2012), using low- and high-Ti basalt averages as the starting composition, was applied to simulate magma evolution through crystal fractionation. The outline of the isobaric calculations spanning temperatures between 1200 and 900°C, at high pressure (1 kbar), low pressure (1 bar) and under three redox conditions (QFM-1, QFM, and QFM+1) are indicated by dashed lines. Faroe Island basalt data are taken from Holm et al. (2001) and Søgner and Holm (2011). Samples IBO1-1 and GOT12 are not shown because of their high calcite content. Key in panel (f), colors represent different rock types and symbols represent fault zones. DZ, damage zone; cc, cataclasite; IBO, Í Botni; GOT, Gøtugjógv; SEL, Selatrað.

dominantly fault internal redistribution of  $\text{SiO}_2$ ,  $\text{Al}_2\text{O}_3$ ,  $\text{CaO}$ , and LOI. With the exception of the calcite-cemented breccia (not shown in plots), all samples fall on a linear trend intersecting the isocon around the position of host rock composition. The most distal damage zone rocks are relatively depleted of mobile elements, and zeolite veins are strongly enriched; cataclasites and breccia plot in between.  $\text{K}_2\text{O}$  shows increasing enrichment from veins to cataclasite and breccia, and further to damage zone samples relative to host rock, with the most significant enrichment in sample GOT21.  $\text{K}_2\text{O}$  is mainly contained in illite and celadonite, which are associated with amygdale linings and thus the primary porosity of the protolith. The host rock sample derives from a massive lava core with minimal porosity, and consequently low  $\text{K}_2\text{O}$  concentration. All other elements plot along their respective isocon, with normalized concentrations decreasing progressively from the damage zone through cataclasites and breccias to veins.

Trace element concentrations generally follow the same trend as Zr. The only exceptions are Ba and Sr, as well as in some cases Cr, Sc, V, and Ni (Figure 14). Elevated Ba/Zr ratios indicate Ba enrichment in the Gøtugjógv damage zone, especially in the hanging wall. In the more mineralized samples, such as breccias and veins, the absolute concentrations of Ba and Zr are reduced due to the addition of zeolite/calcite cement, but the Ba/Zr ratios remain similar. Similar trend can be observed for Sr in Gøtugjógv. Í Botni fault rocks show only slightly elevated Sr, Sc, and Ni in the calcite cemented fault rock breccia. Similarly, calcite-dominated rocks from Gøtugjógv have high Cr, Sc, and V. In the Selatrað fault rocks, Ba and Sr are slightly depleted, and Cr and Sc are strongly enriched in the ultracataclasite. Ba and Sr (and perhaps Cr) correlate with Fe concentration, while V and Sc correlate with Ca. It should be noted that Ba concentration in the Gøtugjógv host rock is about half the concentration of published Faroe Island basalt data (Søgner & Holm, 2011) as well as 1/3–1/5 of the concentrations in Í Botni and Selatrað, respectively.

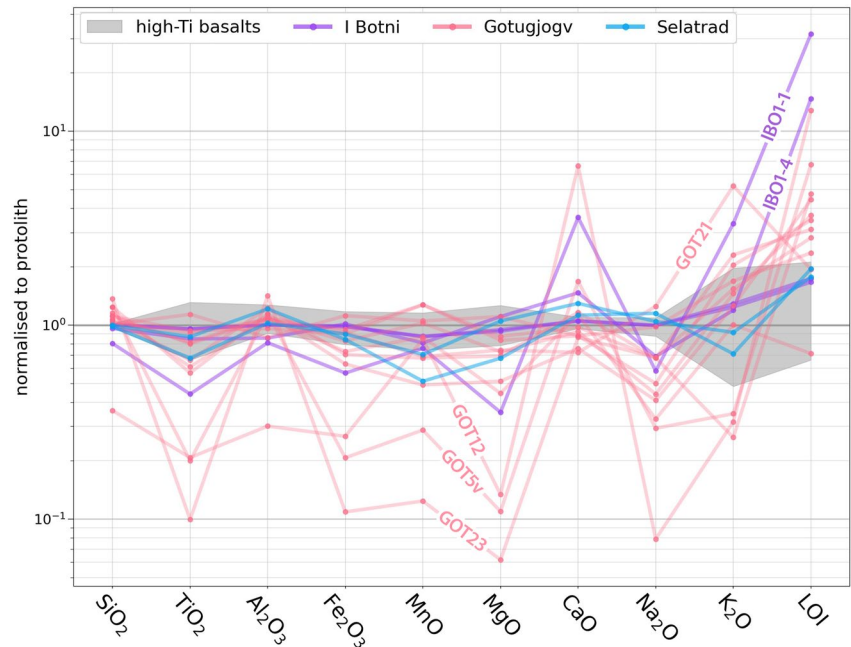


**Figure 9.** Composition of fault rock samples normalized to their respective host rocks (mean IBO host, GOT13, SEL2) and high-Ti basalts on the Faroe Islands (Holm et al., 2001; Søger & Holm, 2011) normalized to the mean composition of the high-Ti basalts. Only zeolite-cemented fault veins (GOT23 and GOT5v) and calcite-cemented fault veins (GOT12 and IBO1-1) show strong deviations.

#### 4.3.2. Element Distribution in Minerals (SEM-EDS)

All samples show almost complete olivine and glass breakdown and replacement by chlorite, mixed smectite, and unidentified phases. These secondary phases have high concentrations of Fe and Mg.

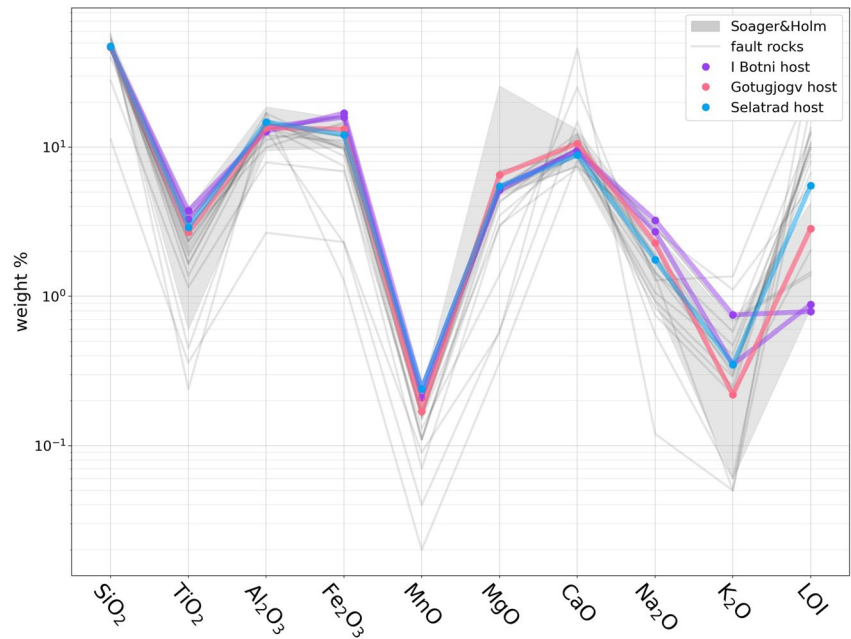


**Figure 10.** Major element composition of protolith sample used for each fault zone and published data for different basalts from the Faroe Islands (Søger & Holm, 2011) and fault rock samples. Note that all protoliths plot at the upper end of the  $\text{TiO}_2$  range and lower end of the MgO range.

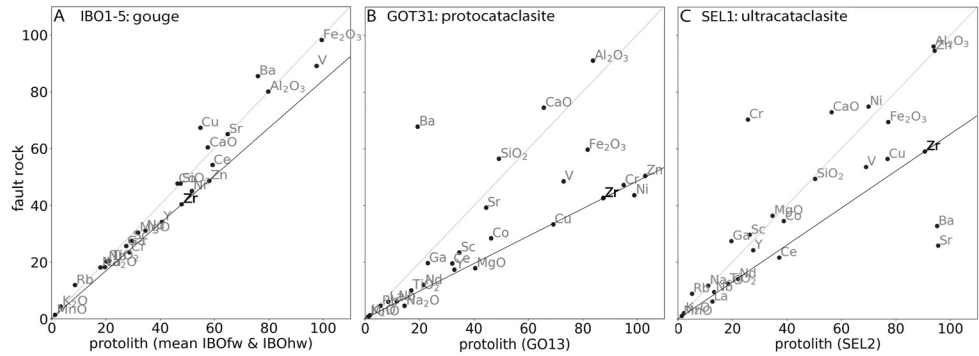


**Figure 11.** Representative isocon diagrams from each fault zone, plotting fault rock against protolith compositions. The selected protolith samples are the most pristine rock that was accessible at each fault zone. The black isocons connecting immobile elements plot below the light gray constant mass reference line, indicating mass gain in all three samples. Isocon diagrams for all analyzed samples can be found in the digital supplement.

In the damage zone, Na is strongly concentrated in analcime at the expense of plagioclase, which is partially replaced. Ca concentration is not increased in the remnants of plagioclase compared to unaltered plagioclase; however, anorthite/albite ratios increase from 1.1 in host rock to  $\leq 3.1$  in the fault core, consistent with preferential dissolution of albite. Only about 30%–40% of plagioclase is replaced by analcime. Besides plagioclase, Ca is concentrated in heulandite/clinoptilolite (which form a continuous solid solution series and are referred to as Ca-zeolite in the following) and other zeolite phases (excluding analcime), filling vesicles or replacing plagioclase closer to the fault core. Zeolites tend to have a higher Si and a lower Al concentrations than plagioclase. The volcanic glass and secondary minerals filling the interstitial space between plagioclase and pyroxene grains

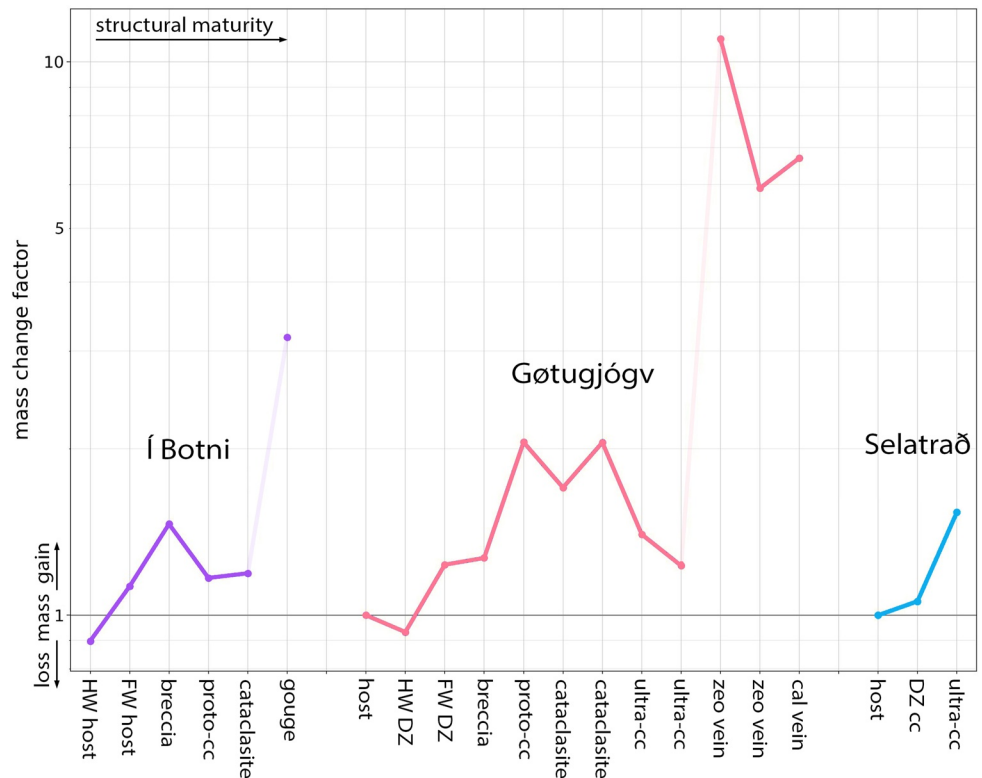


**Figure 12.** The global mass change compared to local protolith ( $M^A/M^0$ , Equation 1). Protoliths are mean IBO host, GOT13, and SEL2. Values  $< 1$  denote mass loss (e.g., leaching), whereas values  $> 1$  denote mass gain (e.g., cementation). Sample names in Table 1. Cal, calcite; cc, cataclasite; DZ, damage zone; FW, footwall; HW, hanging wall; zeo, zeolite.

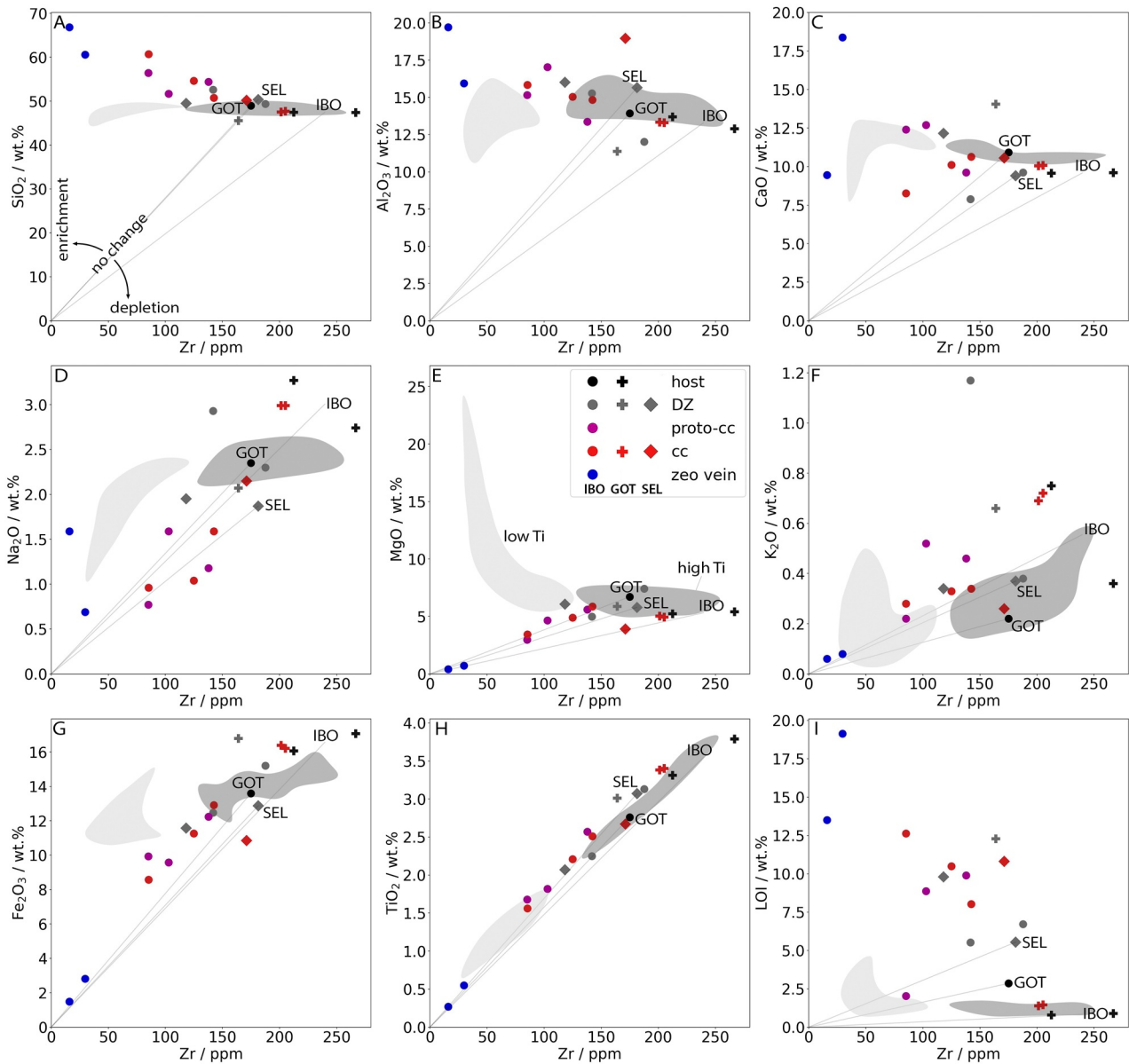


**Figure 13.** Covariance plots for major elements and immobile Zr visualize element mobility during alteration. The isocon connecting the origin with the protolith approximates the path for isochemical evolution from the protolith, samples plotted below are depleted in the studied element and samples plotted above are enriched. Only Si, Al, and Ca show significant deviations from the isocon, indicating that these elements are mobilized during fault rock alteration. They are depleted in the damage zone and enriched in the fault core and zeolite fault veins. Samples IBO1-1 and GOT12 are not shown in the plots because of their high calcite content. The composition of Faroese basalts taken from Holm et al. (2001) and Søger and Holm (2011) is plotted in light (low-Ti) and dark (high-Ti) gray fields. Key in panel (e), colors represent different rock types and symbols represent fault zones. DZ, damage zone; cc, cataclasite; IBO, Í Botni; GOT, Gøtugjógv; SEL, Selatrað.

(or remnants) have variable compositions, either similar to Fe-Ca-pyroxene or a Na-Ca-zeolite. Mg concentration in pyroxenes remains stable across the entire fault zone. However, Fe/Fe + Mg + Ca in pyroxene decreases by about 10 wt.% from host rock to cataclasite in Í Botni, and then another 10 wt.% to samples from Gøtugjógv and Selatrað, whereas the relative Ca concentration increases by only about 1 wt.%. The only other phases containing Mg are rare saponite and illite/celadonite, the latter also concentrating most of the K.

In the fault core, analcime is absent and Na is only abundant in remnant plagioclase. The remaining Na, as well as K, is contained in very low concentrations in zeolites and unidentified phases of the cataclasite matrix. Ca concentration is more homogeneous across the fault core compared to the damage zone or host rock, as it is relatively evenly distributed between zeolites, smectites, and unidentified phases, and abundant only in pyroxene and

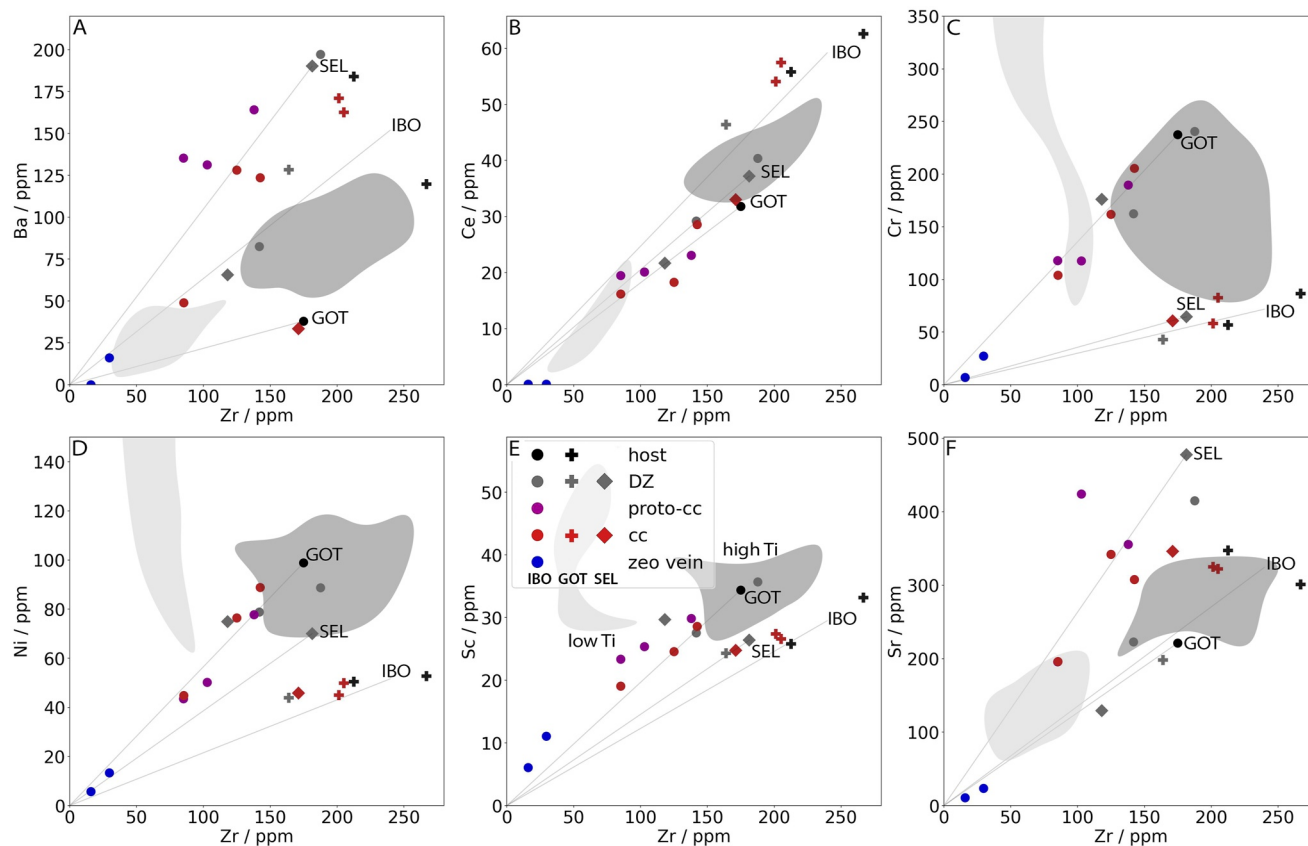


**Figure 14.** Covariance plots for selected trace elements and immobile Zr. Samples IBO1-1 and GOT12 are not shown in the plots because of their high calcite content. Geochemical data for different basalt types (low-Ti in light and high-Ti in dark gray) are taken from Holm et al. (2001) and Søger and Holm (2011). Key in panel (e), colors represent different rock types and symbols represent fault zones. DZ, damage zone; cc, cataclasite; IBO, Í Botni; GOT, Gøtugjógv; SEL, Selatrað.

calcite cements. In fault core breccias, Fe is still chiefly contained in pyroxenes and ilmenite/magnetite, but also secondary phases from glass and olivine breakdown. In the cataclasite matrix, Fe concentration is consistently high, exceeding the concentration in pyroxene. Si is abundant in zeolite grains of the (ultra-) cataclasites, whereas Al is more evenly distributed between zeolites, smectites, and unidentified phases. Ultracataclasites from Gøtugjógv and Selatrað, as well as the cataclasites from Í Botni, have a high concentration of unidentified matrix with no measurable Mg, low Si, but high Al, Ca, and Fe.

## 5. Interpretation and Discussion

### 5.1. Mineralogical Composition and Evolution

Examination of undeformed host rocks indicates that the earliest phase of alteration affects olivine and volcanic glass (Figures 5a–5c), which is common in a wide range of alteration conditions (Frolova et al., 2014; Gislason & Eugster, 1987a; Mattioli et al., 2016). Unaltered olivine is rare in the samples including the protolith (Figure 5a), indicating that its breakdown is diagenetic rather than related to faulting. Olivine replacement minerals are classified as a mixture of saponite and chlorite (Figure 6c), and “pyroxene” which more likely represents a mixed phase analysis (i.e., a mixel) or secondary Fe-Mg silicate (with minor Ca but no Al). Common alteration products of olivine are iddingsite and clay minerals, such as celadonite and nontronite (Alt & Honnorez, 1984; Mattioli et al., 2016).

Volcanic glass and its alteration products are commonly classified as chlorite but show distinct Mg gain, and Si (+Al) loss in fibrous alteration rims compared to the massive cores. Optically, the fibrous rims closely resemble palagonite (Figure 5f), even though the chemical composition does not match such a mixed smectite-zeolite phase. Volcanic glass is at least partially devitrified before deformation-related alteration, based on the zeolitic

cores observed in protolith samples. Fibrous rims (Figure 5a) might be chlorite as suggested by SEM-EDS mineralogy, whereas the green-brown cores are probably another cryptocrystalline Fe-Mg silicate with lower Fe and Mg, and higher Si content than the surrounding chlorite. Volcanic glass is often found to be replaced by aggregates of cryptocrystalline zeolites (Frolova et al., 2014), clays and Fe-oxy-hydroxides (Alt & Honnorez, 1984; Mattioli et al., 2016) or a mixture of those (Ghiara et al., 1993). Unclassified secondary phases resulting from in situ glass devitrification are most likely smectites, zeolites, and Fe-oxy-hydroxides (Gislason & Eugster, 1987a; Hawkins, 1981; Mattioli et al., 2016). The latter are visible in thin sections as opaques (Figure 5c) and might cause the observed brown-red coloration (Figures 5e–5i); the small grain size of these phases inhibits phase identification using SEM-EDS.

Fault rocks representative of early damage are associated with a reduction in relative Fe concentration in pyroxenes (e.g., Í Botni), crossing from pigeonite to augite composition. This released Fe may contribute to red staining within the damage zone and cataclasites (Figures 5e–5i), which we suggest primarily binds onto clay minerals. This is followed by in situ plagioclase zeolitization, first into analcime (incorporating only Na, and releasing Ca) and then also other, more calcic (7–10 wt.% Ca, 1–3 wt.% Na) zeolites around fractures and veins, where more abundant fluids promote element mobility (Figures 5d–5h, 6b<sup>5d–5h</sup>, and 6c). The alteration to analcime only affects about 30%–40% of plagioclase (Figures 6a–6c), possibly limited by the availability of Na.

Fault core rocks, representing initial deformation localization, indicate that analcime and the remaining plagioclase are replaced by more calcic zeolites (Figures 6b and 6c). Similarly, coarse, idiomorphic zeolites (dominantly Ca-zeolite) filled vesicles (Figures 5g and 6c). Stable Na concentrations (Figure 13d) imply that secondary zeolitization scavenges Na locally, probably at the expense of plagioclase and older zeolites. Na concentration should be increased in samples with abundant zeolite if significant amounts were transported by the pore fluid, as is the case for Ca (Figure 13c).

Composition of the brown-red fine-grained matrix in (ultra-) cataclasites is more puzzling. Large areas could not be identified from their EDS spectra (Figure 6e), and the grain size is too small for identification by optical petrography (Figures 5i–5k). The platy to spongy habit observed in the SEM-BSE micrographs (Figure 5j) suggests abundant clay minerals (Frolova et al., 2014; Mattioli et al., 2016) mixed with equant zeolite and pyroxene fragments. However, the matrix contains no Mg (average composition: 5 wt.% Fe, 12 wt.% Al, 22 wt.% Si, 10 wt.% Ca,  $\leq 2$  wt.% Na), which cannot be reconciled with the mineral composition suggested above. Assuming the measured Fe represents small amounts of magnetite or Fe-oxy-hydroxide mixed with the main constituent phase, the remaining chemistry roughly matches a non-specific zeolite composition (with, in atoms per formula unit, 23 O, 13 Al, 7.3 Ca, and 1.9 Na, assuming 72 O in the oxide formula). In this case, the platy/spongy textures observed in SEM-BSE might have resulted from dissolution reactions. Gislason and Eugster (1987a, their Figure 1b) observed similar reaction textures in their dissolution experiments of crystalline basalts, although at 10 $\times$  larger scales.

## 5.2. Pore Fluids

The fault rocks described in this study show evidence of fluid-mediated alteration focused on sites of elevated permeability such as veins and fractures. Groundwater chemistry data are not available for the Faroe Islands (Eidesgaard et al., 2019). The present-day hydrologic system may be similar to that of Iceland or East Greenland, which have a similar geology and geography. In both regions, low-temperature geothermal springs (<150°C) are fed by meteoric water that is thought to form convection zones in fracture and fissure swarms (Arnórsson, 1995b; Hjartarson & Armannsson, 2010). Icelandic low-temperature waters (Table 2) are generally neutral to slightly alkaline (pH 6.1–10.6) and carbonated (<4,100 ppm, but generally between 15 and 60 ppm CO<sub>2</sub>), with similar concentration ranges for SiO<sub>2</sub> (Arnórsson, 1995b; Gislason & Eugster, 1987b). Cation concentrations are low (<20 ppm) except for Na, which typically reaches hundreds-of-ppm (Aggarwal et al., 2000; Arnórsson, 1995b; Arnórsson & Barnes, 1983; Gislason & Eugster, 1987b). High-temperature geothermal fluids (Table 2) have similar cation concentrations, but are slightly acidic and reducing, with H<sub>2</sub>S generally ranging in the tens- to hundreds-of-ppm (Arnórsson, 1995a; Gislason & Eugster, 1987b).

At the time of faulting, the Faroe Islands experienced a much hotter climate as they were emplaced during the Paleocene-Eocene Thermal Maximum, with global temperatures 5–8°C higher than present-day (McInerney & Wing, 2011). Groundwater chemistry in the young Faroe Islands might therefore be more similar to present day

**Table 2**  
*Fluid Composition in Iceland, Hawaii, and the Deccan Traps*

		Temp./°C	pH	HCO <sub>3</sub>	CO <sub>2</sub>	SiO <sub>2</sub>	Ca	Na	Mg	K
Iceland										
Snaefellsnes cold water springs	Arnórsson and Barnes (1983)	4–6	4.5–6.2		616–4,100	5–77	2–256	5–660	1–178	0–27
NE Iceland spring water	Gislason and Eugster (1987b)	2–34	7.7–10.2		18–85	12–93	1–74	89–193	0–22	0–10
High-temp. geothermal waters	Arnórsson (1995a)	181–340	5.3–7.2		154–15,534	271–664	0–1,467	76–9,594	0–1	6–1,480
Low-temp. geothermal waters	Arnórsson (1995b)	7–147	6.1–10.6		1.7–1,358	21–182	1–560	9–486	0–21	0–37
SW Iceland geothermal	Aggarwal et al. (2000)	7–92	6.2–10.7		11–1,101					
Hawaii										
Kilauea summit borehole (NSF)	Tilling and Jones (1991)		7.6–8.7	150–1,080	20–35	67–180	36–106	214–769	22–110	43–142
Hawaii flank borehole (KP-1)	Thomas et al. (1996)		7.5–7.9	61–140		9–39	76–478	1,740–11,700	224–1,320	67–398
Kilauea summit borehole (NSF)	Hurwitz et al. (2003)	73–92	6.7–8.7			107–173	77–162	548–838	366–737	151–245
Deccan Traps										
Jalna groundwater	Kale et al. (2021)	21–32	7.0–9.0	182–970			5–54	34–261	2–46	0–21

Note. All concentrations are in ppm.

Hawaii or the Deccan Traps. Groundwater samples collected in a borehole on the summit of Kilauea (Table 2) are slightly alkaline (pH ~8) and have higher cation concentrations than Icelandic geothermal waters and similar concentration ranges for SiO<sub>2</sub> and carbonate (reported in HCO<sub>3</sub>) (Hurwitz et al., 2003; Tilling & Jones, 1991). They are thought to form through mixing of meteoric groundwater and magmatic gas (Hurwitz et al., 2003). At the coast, groundwater composition (Table 2) only marginally deviates from seawater, with enrichment limited to SiO<sub>2</sub> (Thomas et al., 1996). In the Deccan Traps, groundwater (Table 2) have similar acidity and HCO<sub>3</sub> concentration, while cation concentrations tend to be on the lower end of the concentration spectrum from Kilauea (Kale et al., 2021). We observed strong enrichment of Ba and Sr in the Faroese damage zones compared to the protolith (Figures 14a and 14f). This suggests that pore fluids might be of meteoric origin and percolated down through the highly fractured damage zone. Ba and Sr would be mobilized during plagioclase and matrix breakdown and transported along the fault during downward flow in the damage zone until they are incorporated into secondary phases such as clays and Fe-oxy-hydroxides (Das & Krishnaswami, 2006). Ba has been found to accumulate in the matrix and, to a smaller degree, in plagioclase phenocrysts (Bindeman & Davis, 2000; Philpotts & Schnetzler, 1970). Sr is thought to dissolve from primary basalt phases, especially feldspar and volcanic glass at shallow depth, and then accumulate in zeolites of the heulandite-stilbite zone, resulting in a vertical gradient (Neuhoff et al., 2000). Since Ba and Sr are precipitated in the damage zone, they are depleted in cement of the fault core precipitating later-on.

Alternative fluid sources would be seawater or upwell geothermal fluids. Our data do not show increasing Na-concentrations in altered rocks, which could be expected if they were reacting with fluids similar to the seawater-derived groundwater in Hawaii (Thomas et al., 1996). Hot geothermal fluids in Iceland are reducing due to high H<sub>2</sub>S concentrations (Arnórsson, 1995a). However, virtually no SO<sub>3</sub> is found in our samples (Table 1), and red staining indicates oxidizing conditions in the fault zone. The major element concentration in the fault zone deviates significantly from host basalt only in zones that contain abundant mineral cement (Figures 9 and 13). Even there, only CaO, SiO<sub>2</sub>, and Al<sub>2</sub>O<sub>3</sub> are enriched, and LOI is similarly elevated. Element mobility diagrams (Figures 13 and 14) show that fault rocks consistently plot between two endmember compositions: altered damage zone (e.g., GOT34) and pure zeolite (±calcite) vein (e.g., GOT23), showing that cementation is the only notable chemical influence after the initial host rock alteration. Mineral cements are dominantly calcite and Ca-zeolite

(Figures 5n–5p and 6a), hinting at the presence of a carbonated fluid. As fault rocks from the low-displacement fault in Í Botni only contain calcite cements (Figure 6a), and calcite is also the dominant cement in the fault-distal damage zone in Gøtugjógv and Selatrað, we infer that the pore fluid initially contains relatively high carbonate concentrations. Carbonated, low-temperature groundwater are common in Iceland (Aggarwal et al., 2000; Arnórsson, 1995b; Arnórsson & Barnes, 1983; Gislason & Eugster, 1987b), which has a similar geological setting to the Faroe Islands. Zeolite precipitation would only be possible after significant dissolution of Si and Al during damage zone alteration. A likely source for these elements is volcanic glass, where we can observe a distinct Si and Al loss from the potentially unaltered cores to the fibrous secondary minerals in the rims. This is supported by studies indicating order-of-magnitude higher dissolution rates for basaltic glass compared to crystalline basalt or its mineral components (e.g., Gislason & Eugster, 1987a), and the onset of volcanic glass dissolution is accelerated in carbonated, alkaline fluids (Hawkins, 1981), such as those found in Iceland. As Ca does not accumulate in remnant plagioclase during replacement with analcime, which only incorporates Na, it must be released into the fluid. The same reaction also produces Si and Al as by-products. Basaltic glass dissolution has also been proposed as a source for Ca, Al, and Si, triggering zeolite mineralization in oceanic basalts (Alt & Honnorez, 1984; D'Antonio & Kristensen, 2005) as well as altered basalts in Scotland (Triana et al., 2012).

As indicated by the element mobility diagrams (Figure 13), CaO, Si<sub>2</sub>O, and Al<sub>2</sub>O<sub>3</sub> are transported from the damage zone to the fault core, where they are sequestered in zeolite and calcite cements. The lack of evidence for any external chemical input other than CO<sub>2</sub> and water suggests that the fault core may trap fluids. This is also supported by permeability measurements on basalt-derived fault rocks from the Faroe Islands, which show a high potential for cross-fault sealing with low permeability zones between the host rock and damage zone, and again between damage zone and fault core (Walker, Holdsworth, Armitage, & Faulkner, 2013; Walker, Holdsworth, Imber, et al., 2013). This sets the faults on the Faroe Islands apart from the more widely studied upper-crustal suboceanic faults with strong hydrothermal overprinting (Agar, 1990; Hayman & Karson, 2007, 2009), or faults in deep sheeted dyke complexes (Varga et al., 1992), or (serpentinized) suboceanic gabbro (Boschi et al., 2006; Zihlmann et al., 2018), which all record hydrothermal overprinting and significant deviation from the protolith composition. Leaching of a large volume of damage zone rocks should release enough Ca, Si, and Al for the spatially limited cementation of the fault core (explored further in the next section). Alternation between zeolite and calcite precipitation is probably linked to evolving carbonate activity in the fluid (Neuhoff et al., 2000; Zen, 1961). Early calcite precipitation in Í Botni and replacement of plagioclase with Na-zeolite (i.e., analcime) in Gøtugjógv indicate an initially high carbonate activity, preventing the precipitation of Ca-zeolites (Neuhoff et al., 2000; Zen, 1961). Parts of the damage zone that are assimilated into the fault core become hydraulically isolated by the surrounding impermeable cataclasites, limiting fluid exchange and pressure equilibration. Carbonate activity would be reduced progressively as plagioclase and volcanic glass alteration releases Ca, Si, and Al into the fluid, and calcite precipitates. As a result, conditions would become more favorable for Ca-zeolite precipitation. However, as zeolite cementation removes significant amounts of Ca, Si, and Al from the fluid, especially following hydrofracture, carbonate activity would rise again, and the remaining porosity is filled with calcite. Ca-zeolites are the dominant precipitate as long as its components are sufficiently concentrated in the fluid, but through their depletion carbonate activity increases and eventually prevents further zeolite precipitation. Zeolite precipitation tends to remove silica faster from the solution than it is being released from volcanic glass (Hawkins, 1981). At this stage, calcite is deposited until one of its building blocks is exhausted, leaving a pore fluid that is depleted in all mobile species.

As we see evidence for repeated alternation between calcite and zeolite cementation in the fault cores (Figures 5n–5p), a mechanism controlling the phase that is precipitated is needed, as well as one that allows for the replenishment of the solutes (i.e., Ca, Al, Si, CO<sub>2</sub>) following a hydrofracture and cementation event. The transition from zeolite to calcite precipitation is probably controlled by increasing carbonate activity in the evolving fluid (Neuhoff et al., 2000; Zen, 1961), as outlined above. A potential mechanism for replenishing solutes is partial reassimilation of zeolites and calcite (and potentially other mineral phases) through pressure-solution during and/or following cataclastic creep. The thick layers of cataclasites around slip surfaces suggest that most displacement in the fault core is accommodated by cataclastic creep, which is often accompanied by pressure-solution (e.g., Gratier et al., 2014; Hadizadeh, 1994) of mobile phases such as calcite and zeolites. Several samples, such as Í Botni breccias and some cataclasite from Gøtugjógv and Selatrað show discontinuous and curved foliae defined by the accumulation of clays and opaques and could be interpreted as pressure-solution seams (Figures 5e and 5l). High mobility of the otherwise immobile Al in the fault zones seems surprising at first, but can be explained in

the light of the petrological evolution of the fault rocks. Initial mobilization occurs during metasomatic replacement of plagioclase with much less stable analcime and Ca-zeolite. These zeolites could then be repeatedly dissolved through pressure-solution and reprecipitated during episodic hydrofracture. Various degrees of zeolite dissolution in creeping cataclasites could potentially also explain the variable concentration of residual clays in the matrix of (ultra-) cataclasites. However, these compositional inconsistencies could also have arisen from local variability in protolith composition (e.g., fault veins yielding more zeolite, and assimilated damage zone rocks yielding more clay). Processes for fluid replenishment that lack a mechanism for cement dissolution, such as fluid influx from an external source, would lead to a progressive dilatation of the fault core and the increasing dilution of residual basalt alteration products by Ca, Si, and Al at increasing displacements, which is not supported by our data (Figures 12–14).

Finally, the lack of evidence for fluid replenishment in the fault cores implies that failures or potential ruptures of the fault zone are limited to the fault core, and do not typically breach the core–damage zone boundary, as this would result in fluid ingress from the permeable damage zone. Hence, mature faults in basalts should present a relatively stable, hydrologically closed system and act as quasi-permanent barriers to cross-fault fluid flow. Such a permeability structure is corroborated by permeability measurements of Faroese fault rocks (Walker, Holdsworth, Armitage, & Faulkner, 2013; Walker, Holdsworth, Imber, et al., 2013).

### 5.3. Mass Balance

If a fault core remains hydrologically sealed during its evolution, the gross budget of solutes must balance out across the sealed fluid cell in the fault zone. The mass change factors of individual elements  $T_m$ , as plotted in the element mobility graphs (Figure 13), can be used to calculate the volume of leached damage zone material necessary to balance enrichment in the fault core.

$$T_m = \left( \frac{C_i^0}{C_i^A} \frac{C_j^A}{C_j^0} \right) - 1 \quad (2)$$

where  $C_i$  is the concentration of the immobile element and  $C_j$  is the concentration of the mobile element in the altered fault rock ( $C^0$ ) and protolith ( $C^A$ ) (Ague, 1991; Grant, 1986).

Since we cannot appreciate the lateral extent of fluid cells from our data, we can only calculate a balance across a one-dimensional section of the fault zone, in which we use the thickness of each sampled subzone instead of volume. In this way, we can estimate the necessary thickness of leached rock by comparing the sum of the mass change factor in each subzone weighted by the subzone's width ( $W_{\text{zone}}$ ) from all subzones that gained the considered species (i.e., positive mass change factor) to all the subzones that lost the species (i.e., negative mass change factor).

$$\sum_{\text{enriched}} T_{m,\text{zone}} \times W_{\text{zone}} + \sum_{\text{leached}} T_{m,\text{zone}} \times W_{\text{zone}} = 0 \quad (3)$$

In the Gøtugjógv fault zone, this suggests that  $\text{SiO}_2$  mobilization in about 12 m of the damage zone is required to balance the enrichment through zeolite mineralization in the core and near the damage zone (Table 3). Similar calculations suggest that about 4 and 11 m of the damage zone could provide the  $\text{Al}_2\text{O}_3$  and CaO required to balance their enrichment in the fault core (see digital supplement for calculation). The true thickness for CaO is likely to be lower as we have included a relatively pure, 5 cm wide calcite vein in our calculations to provide an upper bound, but calcite veins in the fault zones usually contain significant amounts of zeolite and clasts (Figure 3c), which reduces their Ca concentration. It should also be noted that the thicknesses we calculated are very rough estimates, since we assumed a homogeneous mass change factor for each subzone, but their heterogeneity is likely to resemble the microtextural complexity of fault rocks. Nevertheless, leaching of a 4–12 m wide damage zone is possible in Gøtugjógv, where the total width of the damage zone is around 13 m.

### 5.4. Depth of Faulting

Amygdaloids in the analyzed fault rocks are almost exclusively filled by a thin lining of celadonite and less abundant smectites, followed by coarse heulandite/clinoptilolite toward the center (Figures 5g and 6c), which is also

**Table 3**  
Mass Balance Calculation for SiO<sub>2</sub> Across a Section of the Götugjógv Fault Zone Using Equation 3

SiO <sub>2</sub> enrichment in					SiO <sub>2</sub> leaching from				
structure	sample	$T_{SiO_2} \times W / m$		$= M_{SiO_2}$	structure	sample	Total $M_{SiO_2} / T_{SiO_2}$		$= W / m$
near DZ	GOT21	0.29	0.30	0.09					
breccia	GOT22	0.31	1.50	0.46					
protocataclasite	GOT31	1.29	0.10	0.13					
cataclasite	GOT33	1.39	0.05	0.07					
					→				
cataclasite	GOT5cc	0.44	0.30	0.13	far DZ	GOT34	1.17	-0.10	-11.97
ultracataclasite	GOT26	0.21	0.05	0.01					
zeo vein	GO5Tv	5.08	0.05	0.25					
cal vein	GOT12	0.59	0.05	0.03					
<b>Total</b>			2.40	1.17					

Note. SiO<sub>2</sub> is leached from the far damage zone and enriched in the near damage zone and fault core. Summing the mass change factors ( $T_{SiO_2}$ ) in the enriched subzones weighted by the subzones' width ( $W$ ) gives the total amount of SiO<sub>2</sub> that has been mobilized ( $M_{SiO_2}$ ; left-hand table). Dividing this by the mass change factor in the depleted far damage zone yields the width of leached damage zone required to balance SiO<sub>2</sub> redistribution (11.97 m; right-hand table). Cal, calcite; DZ, damage zone; zeo, zeolite.

the most common cement in the fault zone (Figure 6). Heulandite and clinoptilolite have been found to destabilize around the same temperature (ca. 450°C and 450–550°C) in laboratory experiments (Ghiara et al., 1999), which might suggest that clinoptilolite in our samples is stable in the same temperature range. This would place the fault zones in the heulandite/stilbite stability zone, from 90–100°C to 110–130°C (Jørgensen, 2006; Kristmannsdóttir & Tomasson, 1978). Illitization of smectite minerals, which is commonly used for temperature estimation (Pytte & Reynolds, 1989; Velde & Vasseur, 1992), is most likely inhibited by the low availability of K in the study area. Using these temperature ranges and geothermal gradients proposed by Jørgensen (2006), ranging from 56°C/km in the Enni formation to 66°C/km in the Beinissvørð Formation, combined with estimated timing of faulting (syn-volcanic for Í Botni, post-volcanic for Götugjógv and Selatrað; Walker et al., 2011) fault cement and amygdale fills would have precipitated at depths of 1.4–2.0 km in Í Botni and 1.5–2.1 km in Götugjógv and Selatrað. This is slightly deeper than expected from zeolite mapping performed by Jørgensen (2006), which would place Í Botni and Götugjógv in the shallower mesolite zone between 1.0 and 1.5 km. Notably, our analysis did not reveal any mesolite in the samples, even though it is compositionally closer to plagioclase than analcime, which forms during the first stage of zeolitization. Fault-parallel fluid migration could potentially modify the geothermal gradients within fault zones. Upward welling of hot hydrothermal fluids could result in an increased gradient, whereas downward percolation of meteoric water could reduce the gradient. In the case here, the latter is more likely and could therefore imply that the faults were active at slightly greater depth than suggested above.

### 5.5. Implications for Fault Evolution

The studied fault zones cut through plagioclase-pyroxene dominated basalts with minor, diagenetically altered olivine, and partially devitrified volcanic glass (Figures 5a–5c and 6b). We apply a space for time substitution for fault rock assemblages to summarize observations into a conceptual fault zone evolution model (Figure 15).

In the incipient fault zone (or at the edge of the damage zone), damage accumulation increases permeability and fluid-rock ratios (Bamberg et al., 2022). Meteoric, carbonated, and slightly alkaline water percolates along the damage zone, where it catalyzes the early metasomatic alteration. Initially, Na-rich plagioclase is replaced by analcime, and volcanic glass continues to break down into smectites, zeolites, and Fe-oxy-hydroxides (Figures 5c–5h, 6b<sup>5c–5h</sup>, and 6c). This releases Ca, Al, and Si into the fluid (Figure 13) and leads to chemical weakening of the

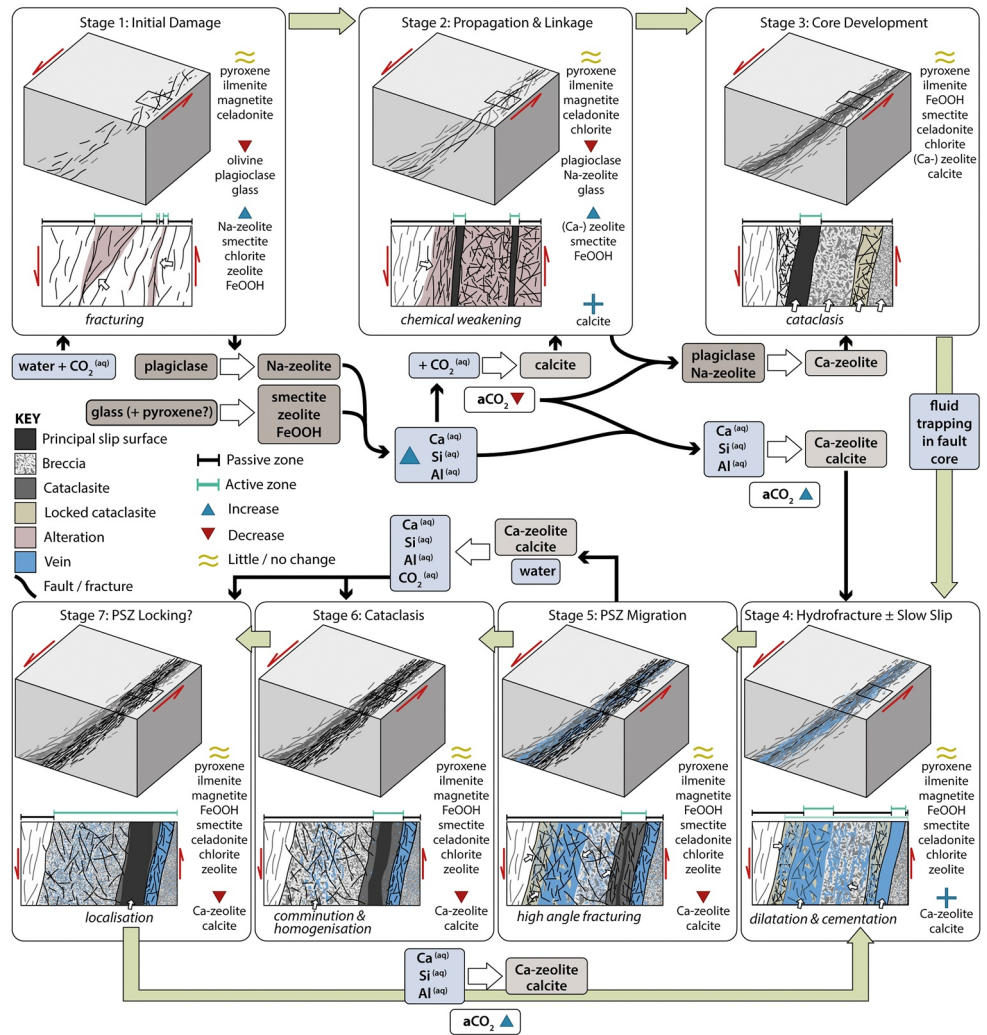


**Figure 15.** A conceptual model of fault evolution outlining the relative timing of petrologic alteration building on the structural model from Bamberg et al. (2022). The damage concentration in the early fault or damage zone increases permeability and thus fluid availability (Stage 1). The alteration of primary phases such as volcanic glass and plagioclase with carbonated waters releases Si, Al, and Ca into the fluid (Stage 1–2). As a result, the carbonate activity in the evolving fluid drops and the primary precipitates change from analcime (Na-zeolite) and calcite to Ca-zeolites (Stage 2–3). Low-permeability shear bands of comminuted and pervasively altered cataclasites trap fluids in the fault core, isolating the fault-internal fluid system (Stage 3). Ongoing shear increases internal fluid pressure, eventually triggering hydrofracture and rapid cementation with zeolites (Stage 4), which strengthen the core and force slip zone migration (Stage 5). Cataclastic creep in the new slip zone is accompanied by pressure-solution of calcite and zeolite cement, replenishing solutes in the fluid (Stage 6–7) and setting up the fault for the next pulse of hydrofracture and cementation (Stage 4).  $a\text{CO}_2$ ,  $\text{CO}_2$  activity; s, solid; aq, aqueous.

rocks (Frolova et al., 2014). Carbonate activity is reduced in the evolving fluid through calcite precipitation and mineral dissolution until Ca-zeolites become the dominant precipitate. The weakened rock localizes deformation into a principal slip zone, establishing a fault core where displacement is accommodated by cataclastic flow (Figures 2b, 2e–2g, 5i, 6d, and 6e). Cataclastic comminution and the potential accumulation of smectites reduce permeability, compartmentalizing the fault zone. Since fluids are now trapped in the core, chemical exchange and pressure equalization with the damage zone are inhibited (Figure 13). Fluids become pressurized due to compaction, eventually triggering hydrofracture (Proctor et al., 2020) and rapid cementation of the fault core (Figures 3b, 3c, 3f, and 5m–5p). Zeolite precipitation depletes dissolved Si, Al, and possibly Ca, increasing carbonate activity in the fluid, and the remaining voids are filled with coarse calcite (Figures 5n–5p). Widespread cementation strengthens the core, forcing the slip zone migration into a weaker domain (Bamberg et al., 2022). The abandoned

slip zone is reworked by cataclasis (Figures 3d and 3e) (Bamberg et al., 2022) while pressure-solution could dissolve some of the cement and replenish solutes in the fluid. Communitation and cement dissolution reset the stage for a subsequent hydrofracture event, and the fault zone continues to evolve through episodic cycles of cementation-strengthening and shear-compaction (Bamberg et al., 2022) with the only significant mineralogical changes being cement precipitation and dissolution.

## 6. Conclusions

Basalt-hosted fault zones in the Faroe Islands are sites of intense petrological alteration, featuring almost complete textural and mineralogical breakdown of the tholeiitic protolith. Olivine and volcanic glass alteration starts during diagenesis, but the primary phases are only completely replaced in damage zone breccias, where damage concentration increases fluid-rock ratios. Olivine is replaced by smectite, chlorite, and an unidentified Fe-Mg silicate that can incorporate some Ca. Volcanic glass is replaced by aggregates of zeolite, smectite, and Fe-oxy-hydroxides. In the vicinity of the fault core, zeolites replace plagioclase. Zeolitization progresses through two stages, where Na-rich plagioclase is replaced by analcime, followed by Ca-zeolites replacing the remaining anorthite-dominated plagioclase and analcime. Only pyroxene and ilmenite/magnetite remain relatively unaltered. In the fault core, secondary phases, pyroxene, and ilmenite/magnetite are mechanically mixed through cataclasis. After the incorporation of water and CO<sub>2</sub>, chemical mobility is limited to alternating Ca-zeolite and calcite precipitation and dissolution, the latter probably by pressure-solution during cataclastic creep in the core. The only mobile species are Ca, Si, Al, and CO<sub>2</sub>. Carbonate is most likely added through meteoric waters percolating through the damage zone, whereas the fault cores appear to be largely hydrologically sealed, inhibiting chemical exchange or fluid-pressure equilibration with the damage zone and host rock.

## Data Availability Statement

High resolution versions of all figures, geochemical data (XRF raw data and reference analyses) and SEM-BSE and EDS maps (incl. mineral maps, element concentration heat maps, and tabulated chemical composition of each raster point) of the samples are available in the Open Science Framework repository (Bamberg, 2023).

## Acknowledgments

We thank Tom Knott and Leon Hicks for their technical support on the SEM, and Lin Marvin-Dorland for her help during XRF analysis. We also wish to thank Catriona Menzies, David Holwell, Jeremy Rushton, and Zhenchao Zang, as well as the reviewers Nick Hayman and Jessica Warren for their valuable feedback that greatly improved this manuscript. This work was funded by the College of Science and Engineering of the University of Leicester, UK.

## References

- Agar, S. M. (1990). Fracture evolution in the upper ocean crust: Evidence from DSDP hole 504B. *Geological Society, London, Special Publications*, 54(1), 41–50. <https://doi.org/10.1144/GSL.SP.1990.054.01.04>
- Aggarwal, J., Palmer, M., Bullen, T., Arnórsson, S., & Ragnarsdóttir, K. (2000). The boron isotope systematics of Icelandic geothermal waters: 1. Meteoric water charged systems. *Geochimica et Cosmochimica Acta*, 64(4), 579–585. [https://doi.org/10.1016/S0016-7037\(99\)00300-2](https://doi.org/10.1016/S0016-7037(99)00300-2)
- Ague, J. J. (1991). Evidence for major mass transfer and volume strain during regional metamorphism of pelites. *Geology*, 19(8), 855–858. [https://doi.org/10.1130/0091-7613\(1991\)019%3C0855:EFMMTA%3E2.3.CO;2](https://doi.org/10.1130/0091-7613(1991)019%3C0855:EFMMTA%3E2.3.CO;2)
- Alt, J. C., & Honnorez, J. (1984). Alteration of the upper oceanic crust, DSDP site 417: Mineralogy and chemistry. *Contributions to Mineralogy and Petrology*, 87(2), 149–169. <https://doi.org/10.1007/BF00376221>
- Arnórsson, S. (1995a). Geothermal systems in Iceland: Structure and conceptual models—I. High-temperature areas. *Geothermics*, 24(5), 561–602. [https://doi.org/10.1016/0375-6505\(95\)00025-9](https://doi.org/10.1016/0375-6505(95)00025-9)
- Arnórsson, S. (1995b). Geothermal systems in Iceland: Structure and conceptual models—II. Low-temperature areas. *Geothermics*, 24(5), 603–629. [https://doi.org/10.1016/0375-6505\(95\)00026-7](https://doi.org/10.1016/0375-6505(95)00026-7)
- Arnórsson, S., & Barnes, I. (1983). The nature of carbon dioxide waters in Snaefellsnes, western Iceland. *Geothermics*, 12(2–3), 171–176. [https://doi.org/10.1016/0375-6505\(83\)90027-5](https://doi.org/10.1016/0375-6505(83)90027-5)
- Bamberg, B. (2023). Basaltic fault rock petrology [Dataset]. Open Science Framework. Retrieved from <https://osf.io/r3skf>
- Bamberg, B., Walker, R., Reichow, M., & Ougier-Simonin, A. (2022). Fluid-driven cyclic reorganization in shallow basaltic fault zones. *Geosphere*, 18(5), 1600–1621. <https://doi.org/10.1130/GES02488.1>
- Bindeman, I. N., & Davis, A. M. (2000). Trace element partitioning between plagioclase and melt: Investigation of dopant influence on partition behavior. *Geochimica et Cosmochimica Acta*, 64(16), 2863–2878. [https://doi.org/10.1016/S0016-7037\(00\)00389-6](https://doi.org/10.1016/S0016-7037(00)00389-6)
- Boschi, C., Früh-Green, G. L., Delacour, A., Karson, J. A., & Kelley, D. S. (2006). Mass transfer and fluid flow during detachment faulting and development of an oceanic core complex, Atlantis Massif (MAR 30°N). *Geochemistry, Geophysics, Geosystems*, 7(1), Q01004. <https://doi.org/10.1029/2005GC001074>
- Boulton, C., Moore, D. E., Lockner, D. A., Toy, V. G., Townend, J., & Sutherland, R. (2014). Frictional properties of exhumed fault gouges in DFDP-1 cores, Alpine Fault, New Zealand. *Geophysical Research Letters*, 41(2), 356–362. <https://doi.org/10.1002/2013GL058236>
- Bubeck, A., Walker, R. J., Imber, J., Holdsworth, R. E., MacLeod, C. J., & Holwell, D. A. (2017). Extension parallel to the rift zone during segmented fault growth: Application to the evolution of the NE Atlantic. *Solid Earth*, 8(6), 1161–1180. <https://doi.org/10.5194/se-8-1161-2017>
- Carpenter, B. M., Ikari, M. J., & Marone, C. (2016). Laboratory observations of time-dependent frictional strengthening and stress relaxation in natural and synthetic fault gouges. *Journal of Geophysical Research: Solid Earth*, 121(2), 1183–1201. <https://doi.org/10.1002/2015JB012136>
- Chalmers, J. A., & Waagstein, R. (2006). *Scientific results from the deepened Lopra-1 borehole, Faroe Islands*. Geological Survey of Denmark and Greenland, Danish Ministry of the Environment.

- D'Antonio, M., & Kristensen, M. (2005). Hydrothermal alteration of oceanic crust in the West Philippine Sea Basin (Ocean Drilling Program Leg 195, Site 1201): Inferences from a mineral chemistry investigation. *Mineralogy and Petrology*, 83(1), 87–112. <https://doi.org/10.1007/s00710-004-0060-6>
- Das, A., & Krishnaswami, S. (2006). Barium in Deccan Basalt Rivers: Its abundance, relative mobility and flux. *Aquatic Geochemistry*, 12(3), 221–238. <https://doi.org/10.1007/s10498-005-5856-4>
- Deer, W. A., Howie, R. A., & Zussman, J. (2013). *An introduction to the rock-forming minerals*. Mineralogical Society of Great Britain and Ireland.
- Eidesgaard, Ó. R., Schovsbo, N. H., Boldreel, L. O., & Ólavsdóttir, J. (2019). Shallow geothermal energy system in fractured basalt: A case study from Kollafjörður, Faroe Islands, NE-Atlantic Ocean. *Geothermics*, 82, 296–314. <https://doi.org/10.1016/j.geothermics.2019.07.005>
- Frolova, J., Ladygin, V., Rychagov, S., & Zhubaya, D. (2014). Effects of hydrothermal alterations on physical and mechanical properties of rocks in the Kuril–Kamchatka island arc. *Engineering Geology*, 183, 80–95. <https://doi.org/10.1016/j.enggeo.2014.10.011>
- Gaina, C., Gernigon, L., & Ball, P. (2009). Palaeocene–Recent plate boundaries in the NE Atlantic and the formation of the Jan Mayen microcontinent. *Journal of the Geological Society*, 166(4), 601–616. <https://doi.org/10.1144/0016-76492008-112>
- Gariépy, C., Ludden, J., & Brooks, C. (1983). Isotopic and trace element constraints on the genesis of the Faeroe lava pile. *Earth and Planetary Science Letters*, 63(2), 257–272. [https://doi.org/10.1016/0012-821X\(83\)90041-9](https://doi.org/10.1016/0012-821X(83)90041-9)
- Gernigon, L., Gaina, C., Olesen, O., Ball, P., Péron-Pinvidic, G., & Yamasaki, T. (2012). The Norway Basin revisited: From continental breakup to spreading ridge extinction. *Marine and Petroleum Geology*, 35(1), 1–19. <https://doi.org/10.1016/j.marpetgeo.2012.02.015>
- Ghiara, M., Franco, E., Petti, C., Stanzione, D., & Valentino, G. (1993). Hydrothermal interaction between basaltic glass, deionized water and seawater. *Chemical Geology*, 104(1–4), 125–138. [https://doi.org/10.1016/0009-2541\(93\)90146-A](https://doi.org/10.1016/0009-2541(93)90146-A)
- Ghiara, M. R., Petti, C., Franco, E., Lonis, R., Luxoro, S., & Gnazzo, L. (1999). Occurrence of clinoptilolite and mordenite in Tertiary calc-alkaline pyroclastites from Sardinia (Italy). *Clays and Clay Minerals*, 47(3), 319–328. <https://doi.org/10.1007/s0030200199990470308>
- Ghiorso, M. S., & Sack, R. O. (1995). Chemical mass transfer in magmatic processes IV. A revised and internally consistent thermodynamic model for the interpolation and extrapolation of liquid–solid equilibria in magmatic systems at elevated temperatures and pressures. *Contributions to Mineralogy and Petrology*, 119(2), 197–212. <https://doi.org/10.1007/BF00307281>
- Gislason, S. R., & Eugster, H. P. (1987a). Meteoric water–basalt interactions. I: A laboratory study. *Geochimica et Cosmochimica Acta*, 51(10), 2827–2840. [https://doi.org/10.1016/0016-7037\(87\)90161-X](https://doi.org/10.1016/0016-7037(87)90161-X)
- Gislason, S. R., & Eugster, H. P. (1987b). Meteoric water–basalt interactions. II: A field study in NE Iceland. *Geochimica et Cosmochimica Acta*, 51(10), 2841–2855. [https://doi.org/10.1016/0016-7037\(87\)90162-1](https://doi.org/10.1016/0016-7037(87)90162-1)
- Grant, J. A. (1986). The isocon diagram; a simple solution to Gresens' equation for metasomatic alteration. *Economic Geology*, 81(8), 1976–1982. <https://doi.org/10.2113/gsecongeo.81.8.1976>
- Gratier, J. P., Renard, F., & Vial, B. (2014). Postseismic pressure solution creep: Evidence and time-dependent change from dynamic indenting experiments. *Journal of Geophysical Research: Solid Earth*, 119(4), 2764–2779. <https://doi.org/10.1002/2013JB010768>
- Gualda, G. A. R., & Ghiorso, M. S. (2015). MELTS\_Excel: A Microsoft Excel-based MELTS interface for research and teaching of magma properties and evolution. *Geochemistry, Geophysics, Geosystems*, 16(1), 315–324. <https://doi.org/10.1002/2014GC005545>
- Gualda, G. A. R., Ghiorso, M. S., Lemons, R. V., & Carley, T. L. (2012). Rhyolite–MELTS: A modified calibration of MELTS optimized for silica-rich, fluid-bearing magmatic systems. *Journal of Petrology*, 53(5), 875–890. <https://doi.org/10.1093/ptrology/egr080>
- Hadizadeh, J. (1994). Interaction of cataclasis and pressure solution in a low-temperature carbonate shear zone. *Pure and Applied Geophysics*, 143(1), 255–280. <https://doi.org/10.1007/BF00874331>
- Haines, S. H., Kaproth, B., Marone, C., Saffer, D., & van der Pluijm, B. (2013). Shear zones in clay-rich fault gouge: A laboratory study of fabric development and evolution. *Journal of Structural Geology*, 51, 206–225. <https://doi.org/10.1016/j.jsg.2013.01.002>
- Hald, N., & Waagstein, R. (1991). The dykes and sills of the Early Tertiary Faeroe Island basalt plateau. *Transactions of the Royal Society of Edinburgh Earth Sciences*, 82(4), 373–388. <https://doi.org/10.1017/S0263593300004211>
- Hansen, H., Pedersen, A., Duncan, R., Bird, D., Brooks, C., Fawcett, J., et al. (2002). Volcanic stratigraphy of the southern Prinsen af Wales Bjerger region, East Greenland. *Geological Society, London, Special Publications*, 197(1), 183–218. <https://doi.org/10.1144/GSL.SP.2002.197.01.08>
- Hawkins, D. B. (1981). Kinetics of glass dissolution and zeolite formation under hydrothermal conditions. *Clays and Clay Minerals*, 29(5), 331–340. <https://doi.org/10.1346/CCMN.1981.0290503>
- Hayman, N. W., & Karson, J. A. (2007). Faults and damage zones in fast-spread crust exposed on the north wall of the Hess Deep Rift: Conduits and seals in seafloor hydrothermal systems. *Geochemistry, Geophysics, Geosystems*, 8(10), Q10002. <https://doi.org/10.1029/2007GC001623>
- Hayman, N. W., & Karson, J. A. (2009). Crustal faults exposed in the Pito Deep Rift: Conduits for hydrothermal fluids on the southeast Pacific Rise. *Geochemistry, Geophysics, Geosystems*, 10(2), Q02013. <https://doi.org/10.1029/2008GC002319>
- Hippert, J. (1998). Breakdown of feldspar, volume gain and lateral mass transfer during mylonitization of granitoid in a low metamorphic grade shear zone. *Journal of Structural Geology*, 20(2–3), 175–193. [https://doi.org/10.1016/S0191-8141\(97\)00083-7](https://doi.org/10.1016/S0191-8141(97)00083-7)
- Hjartarson, A., & Armannsson, H. (2010). Geothermal research in Greenland. In *Proceedings World Geothermal Congress, Bali, Indonesia* (pp. 1–8).
- Holm, P. M., Hald, N., & Waagstein, R. (2001). Geochemical and Pb–Sr–Nd isotopic evidence for separate hot depleted and Iceland plume mantle sources for the Palaeogene basalts of the Faroe Islands. *Chemical Geology*, 178(1–4), 95–125. [https://doi.org/10.1016/S0009-2541\(01\)00260-1](https://doi.org/10.1016/S0009-2541(01)00260-1)
- Hurwitz, S., Goff, F., Janik, C. J., Evans, W. C., Counce, D. A., Sorey, M. L., & Ingebritsen, S. E. (2003). Mixing of magmatic volatiles with groundwater and interaction with basalt on the summit of Kilauea Volcano, Hawaii. *Journal of Geophysical Research*, 108(B1), 2028. <https://doi.org/10.1029/2001JB001594>
- Jørgensen, O. (2006). The regional distribution of zeolites in the basalts of the Faroe Islands and the significance of zeolites as palaeotemperature indicators. *Geological Survey of Denmark and Greenland Bulletin*, 9, 123–156. <https://doi.org/10.34194/geusb.v9.4865>
- Kale, A., Bandela, N., Kulkarni, J., Sahoo, S. K., & Kumar, A. (2021). Hydrogeochemistry and multivariate statistical analysis of groundwater quality of hard rock aquifers from Deccan trap basalt in Western India. *Environmental Earth Sciences*, 80(7), 1–24. <https://doi.org/10.1007/s12665-021-09586-7>
- Kristmannsdóttir, H. (1979). *Alteration of basaltic rocks by hydrothermal-activity at 100–300°C*. *Developments in Sedimentology* (Vol. 27, pp. 359–367). Elsevier.
- Kristmannsdóttir, H., & Tomasson, J. (1978). Zeolite zones in geothermal areas in Iceland. In L. B. Sand & F. A. Mumpton (Eds.), *Natural zeolites: Occurrence, properties, use* (pp. 277–284). Pergamon Press.
- Lewis, A. L., Sarkar, B., Wade, P., Kemp, S. J., Hodson, M. E., Taylor, L. L., et al. (2021). Effects of mineralogy, chemistry and physical properties of basalts on carbon capture potential and plant-nutrient element release via enhanced weathering. *Applied Geochemistry*, 132, 105023. <https://doi.org/10.1016/j.apgeochem.2021.105023>

- Marieni, C., Pfikryl, J., Aradóttir, E. S., Gunnarsson, I., & Stefánsson, A. (2018). Towards 'green' geothermal energy: Co-mineralization of carbon and sulfur in geothermal reservoirs. *International Journal of Greenhouse Gas Control*, 77, 96–105. <https://doi.org/10.1016/j.ijggc.2018.07.011>
- Matter, J. M., Stute, M., Snæbjörnsdóttir, S. Ó., Oelkers, E. H., Gislason, S. R., Aradóttir, E. S., et al. (2016). Rapid carbon mineralization for permanent disposal of anthropogenic carbon dioxide emissions. *Science*, 352(6291), 1312–1314. <https://doi.org/10.1126/science.aad8132>
- Mattioli, M., Cenni, M., & Passaglia, E. (2016). Secondary mineral assemblages as indicators of multi stage alteration processes in basaltic lava flows: Evidence from the Lessini Mountains, Veneto Volcanic Province, Northern Italy. *Periodico di Mineralogia*, 85, 1–24. <https://doi.org/10.2451/2015PM0375>
- McInerney, F. A., & Wing, S. L. (2011). The Paleocene-Eocene Thermal Maximum: A perturbation of carbon cycle, climate, and biosphere with implications for the future. *Annual Review of Earth and Planetary Sciences*, 39(1), 489–516. <https://doi.org/10.1146/annurev-earth-040610-133431>
- Neuhoff, P. S., Fridriksson, T., & Bird, D. K. (2000). Zeolite parageneses in the North Atlantic Igneous Province: Implications for geotectonics and groundwater quality of basaltic crust. *International Geology Review*, 42(1), 15–44. <https://doi.org/10.1080/00206810009465068>
- Passéy, S. (2009). Recognition of a faulted basalt lava flow sequence through the correlation of stratigraphic marker units, Skopunarfjörður, Faroe Islands. In T. Varming & H. Ziska (Eds.), *Faroe Islands Exploration Conference: Proceedings of the 2nd Conference* (Vol. 50, pp. 174–204). Annales Societatis Scientiarum Færoensis.
- Passéy, S. R., & Bell, B. R. (2007). Morphologies and emplacement mechanisms of the lava flows of the Faroe Islands Basalt Group, Faroe Islands, NE Atlantic Ocean. *Bulletin of Volcanology*, 70(2), 139–156. <https://doi.org/10.1007/s00445-007-0125-6>
- Passéy, S. R., & Jolley, D. W. (2008). A revised lithostratigraphic nomenclature for the Palaeogene Faroe Islands Basalt group, NE Atlantic Ocean. *Earth and Environmental Science Transactions of the Royal Society of Edinburgh*, 99(3–4), 127–158. <https://doi.org/10.1017/S1755691009008044>
- Philpotts, J. A., & Schnetzler, C. C. (1970). Phenocryst-matrix partition coefficients for K, Rb, Sr and Ba, with applications to anorthosite and basalt genesis. *Geochimica et Cosmochimica Acta*, 34(3), 307–322. [https://doi.org/10.1016/0016-7037\(70\)90108-0](https://doi.org/10.1016/0016-7037(70)90108-0)
- Proctor, B., Lockner, D., Kilgore, B., Mitchell, T., & Beeler, N. (2020). Direct evidence for fluid pressure, dilatancy, and compaction affecting slip in isolated faults. *Geophysical Research Letters*, 47(16), e2019GL086767. <https://doi.org/10.1029/2019GL086767>
- Pytte, A., & Reynolds, R. (1989). *The thermal transformation of smectite to illite, Thermal history of sedimentary basins* (pp. 133–140). Springer.
- Rasmussen, J., & Noe-Nygaard, A. (1970). *Geology of the Faeroe Islands: (Pre-Quaternary)*. CA Reitzels.
- Ritchie, J., & Hitchen, K. (1996). Early Paleogene offshore igneous activity to the northwest of the UK and its relationship to the North Atlantic Igneous Province. *Geological Society, London, Special Publications*, 101(1), 63–78. <https://doi.org/10.1144/GSL.SP.1996.101.01.04>
- Schenato, F., Formoso, M., Dudoignon, P., Meunier, A., Proust, D., & Mas, A. (2003). Alteration processes of a thick basaltic lava flow of the Paraná Basin (Brazil): Petrographic and mineralogical studies. *Journal of South American Earth Sciences*, 16(5), 423–444. [https://doi.org/10.1016/S0895-9811\(03\)00098-1](https://doi.org/10.1016/S0895-9811(03)00098-1)
- Shimamoto, T., & Logan, J. M. (1981). Effects of simulated fault gouge on the sliding behavior of Tennessee sandstone: Nonclay gouges. *Journal of Geophysical Research*, 86(B4), 2902–2914. <https://doi.org/10.1029/JB086iB04p02902>
- Snæbjörnsdóttir, S. Ó., Sigfússon, B., Marieni, C., Goldberg, D., Gislason, S. R., & Oelkers, E. H. (2020). Carbon dioxide storage through mineral carbonation. *Nature Reviews Earth and Environment*, 1(2), 90–102. <https://doi.org/10.1038/s43017-019-0011-8>
- Søager, N., & Holm, P. M. (2009). Extended correlation of the Paleogene Faroe Islands and East Greenland plateau basalts. *Lithos*, 107(3–4), 205–215. <https://doi.org/10.1016/j.lithos.2008.10.002>
- Søager, N., & Holm, P. M. (2011). Changing compositions in the Iceland plume; Isotopic and elemental constraints from the Paleogene Faroe flood basalts. *Chemical Geology*, 280(3–4), 297–313. <https://doi.org/10.1016/j.chemgeo.2010.11.017>
- Stillings, M., Shipton, Z. K., & Lunn, R. J. (2023). Mechanochemical processing of silicate rocks to trap CO<sub>2</sub>. *Nature Sustainability*, 6(7), 780–788. <https://doi.org/10.1038/s41893-023-01083-y>
- Storey, M., Duncan, R. A., & Tegner, C. (2007). Timing and duration of volcanism in the North Atlantic Igneous Province: Implications for geodynamics and links to the Iceland hotspot. *Chemical Geology*, 241(3), 264–281. <https://doi.org/10.1016/j.chemgeo.2007.01.016>
- Thomas, D., Paillet, F. L., & Conrad, M. (1996). Hydrogeology of the Hawaii Scientific Drilling Project borehole KP-1: 2. Groundwater geochemistry and regional flow patterns. *Journal of Geophysical Research*, 101(B5), 11683–11694. <https://doi.org/10.1029/95JB03845>
- Tilling, R. I., & Jones, B. F. (1991). Composition of waters from the research drill hole at summit of Kilauea Volcano and of selected thermal and non-thermal groundwaters, Hawaii.
- Triana, R., Manuel, J., Herrera, R., Francisco, J., Ríos, R., Alberto, C., et al. (2012). Natural zeolites filling amygdaloids and veins in basalts from the British Tertiary Igneous Province on the Isle of Skye, Scotland. *Earth Sciences Research Journal*, 16(1), 41–53.
- Varga, L. B., Varga, R. J., & Schiffman, P. (1992). Relation between ore-forming hydrothermal systems and extensional deformation in the Solea graben spreading center, Troodos ophiolite, Cyprus. *Geology*, 20(11), 987–990. [https://doi.org/10.1130/0091-7613\(1992\)020<0987:Rbofhs>2.3.Co;2](https://doi.org/10.1130/0091-7613(1992)020<0987:Rbofhs>2.3.Co;2)
- Velde, B., & Vasseur, G. (1992). Estimation of the diagenetic smectite to illite transformation in time-temperature space. *American Mineralogist*, 77(9–10), 967–976.
- Waagstein, R., Guise, P., & Rex, D. (2002). K/Ar and <sup>39</sup>Ar/<sup>40</sup>Ar whole-rock dating of zeolite facies metamorphosed flood basalts: The upper Paleocene basalts of the Faroe Islands, NE Atlantic. *Geological Society, London, Special Publications*, 197(1), 219–252. <https://doi.org/10.1144/GSL.SP.2002.197.01.09>
- Waagstein, R., Hald, N., Jørgensen, O., Nielsen, P. H., Noe, A., Jørgensen, O., et al. (1984). Deep drilling on the Faeroe Islands. *Bulletin of the Geological Society of Denmark*, 32, 133–138. <https://doi.org/10.37570/bgsd-1983-32-09>
- Walker, R. J., Holdsworth, R. E., Armitage, P. J., & Faulkner, D. R. (2013). Fault zone permeability structure evolution in basalts. *Geology*, 41(1), 59–62. <https://doi.org/10.1130/G33508.1>
- Walker, R. J., Holdsworth, R. E., Imber, J., & Ellis, D. (2011). Onshore evidence for progressive changes in rifting directions during continental break-up in the NE Atlantic. *Journal of the Geological Society*, 168(1), 27–48. <https://doi.org/10.1144/0016-76492010-021>
- Walker, R. J., Holdsworth, R. E., Imber, J., & Ellis, D. (2012). Fault-zone evolution in layered basalt sequences: A case study from the Faroe Islands, NE Atlantic margin. *GSA Bulletin*, 124(7–8), 1382–1393. <https://doi.org/10.1130/B30512.1>
- Walker, R. J., Holdsworth, R. E., Imber, J., Faulkner, D. R., & Armitage, P. J. (2013). Fault zone architecture and fluid flow in interlayered basaltic volcanoclastic-crystalline sequences. *Journal of Structural Geology*, 51, 92–104. <https://doi.org/10.1016/j.jsg.2013.03.004>
- Winter, J. (2001). *An introduction to igneous and metamorphic petrology*. Pearson.
- Woodcock, N. H., & Mort, K. (2008). Classification of fault breccias and related fault rocks. *Geological Magazine*, 145(3), 435–440. <https://doi.org/10.1017/S0016756808004883>
- Yükselen-Aksoy, Y. (2010). Characterization of two natural zeolites for geotechnical and geoenvironmental applications. *Applied Clay Science*, 50(1), 130–136. <https://doi.org/10.1016/j.clay.2010.07.015>
- Zen, E.-A. (1961). The zeolite facies; an interpretation. *American Journal of Science*, 259(6), 401–409. <https://doi.org/10.2475/ajs.259.6.401>

- Zihlmann, B., Müller, S., Coggon, R. M., Koepke, J., Garbe-Schönberg, D., & Teagle, D. A. H. (2018). Hydrothermal fault zones in the lower oceanic crust: An example from Wadi Gideah, Samail ophiolite, Oman. *Lithos*, 323, 103–124. <https://doi.org/10.1016/j.lithos.2018.09.008>
- Zviagina, B. B., Drits, V. A., & Dorzhieva, O. V. (2020). Distinguishing features and identification criteria for K-dioctahedral 1M micas (illite-aluminoceladonite and illite-glaucoune-celadonite series) from middle-infrared spectroscopy data. *Minerals*, 10(2), 153. <https://doi.org/10.3390/min10020153>

### References From the Supporting Information

- Govindaraju, K. (1994). 1994 Compilation of working values and sample description for 383 geostandards. *Geostandards Newsletter*, 18(S1), 1–158. <https://doi.org/10.1046/j.1365-2494.1998.53202081.x-i1>
- Imai, N., Terashima, S., Itoh, S., & Ando, A. (1995). 1994 compilation of analytical data for minor and trace elements in seventeen GSI geochemical reference samples, "igneous rock series". *Geostandards Newsletter*, 19(2), 135–213. <https://doi.org/10.1111/j.1751-908X.1995.tb00158.x>